Development of High Repetition Rate Cr:LiCAF Femtosecond Lasers and Application of Multipass-Cavity Ti:Sapphire Lasers in THz Generation

A Thesis

Submitted to The Graduate School of Engineering and Science

of

Koç University

In Partial Fulfillment of The Requirements

for

The Degree of

Master of Science

by

Can Cihan

September 2013

Koç University

Graduate School of Sciences and Engineering

This is to certify that I have examined this copy of a master's thesis by

Can Cihan

and have found that it is complete and satisfactory in all respects,

and that any and all revisions required by the final

examining committee have been made.

Committee Members:

_____

Alphan Sennaroğlu, Ph. D. (Advisor)

_____

Ümit Demirbaş Ph. D.

_____

Şükrü Ekin Kocabaş, Ph. D.

Date: _____

ABSTRACT

There is a great deal of interest for developing low-cost, robust, compact and efficient femtosecond lasers for time and frequency domain applications. In recent years, Cr^{3+}-doped colquiriites (Cr:LiSAF, Cr:LiCAF, Cr:LiSGaF) have emerged as promising alternatives to Ti:Sapphire lasers near 800 nm because of numerous favorable laser characteristics. These include the possibility of direct diode pumping with low cost diodes, broad emission bands to generate fs pulses and high quantum efficiency near room temperature.

The first part of this thesis work focuses on the design and experimental demonstration of a directly diode pumped, low cost, and highly efficient 800-nm Cr:LiCAF laser which can be operated above 100 MHz with the goal of developing high repetition rate oscillators for frequency comb applications. In the experiments, a four mirror x-cavity laser containing a 7% doped Cr:LiCAF crystal was endpumped with a recently developed high brightness, 1-W tapered diode at 675 nm. By using 915 mW of pump power, the Cr:LiCAF laser produced 340 fs pulses around 800 nm with an output power of 51 mW, at a repetition rate of 120 MHz. A semiconductor Bragg reflector (SBR) was added into the resonator to initiate the mode-locked operation of the laser. We expect that, with the higher pump powers available from the tapered diode, it should be possible to reach GHz level repetition rates with this resonator for frequency comb applications.

The second part of the thesis work utilizes a home-built multi-pass cavity femtosecond Ti:Sapphire laser, generating 98 fs pulses with a repetition rate of 5.53 MHz at 776 nm, to obtain THz radiation from a photoconductive antenna. The output of the Ti:Sapphire laser with an average power of 60-70 mW power was focused on a low-temperature grown GaAs (Lt-GaAs) structured photoconductive antenna which generated THz waves with a signal strength of 5 mV detected with a second photoconductive antenna. The generated THz waves were in the frequency range of 0.1-0.7 THz. With improved antenna and detection design, we expect to further improve the bandwidth and efficiency of THz generation.

ÖZET

Maliyeti düşük, dayanıklı, kompakt ve verimli fs lazerlerinin geliştirilmesi, zaman ve frekans çerçevesindeki uygulamalar için önem arz etmektedir. Son zamanlarda, Cr^{+3} katkılı colquiriite lazer malzemeleri (Cr:LiSAF, Cr:LiCAF, Cr:LiSGaF) bazı avantajları sayesinde Ti:safir lazerlerine önemli bir alternatif oluşturmuşlardır. Bu avantajlar, maliyeti düşük diyotlarla pompalanmaya elverişli olmaları, geniş ışınım bantlarına sahip olmaları ve oda sıcaklığında yüksek kuantum verimine sahip olmaları olarak sıralanabilir.

Bu tezin ilk kısmında, 100 MHz üzerinde çalışan, daralan kılavuz yapılı diyot ile pompalanan, yüksek güçlü, maliyeti düşük, yüksek verimlilikte çalışan 800nm Cr:LiCAF lazerinin tasarımı ve deneysel sunumu ele alınmıştır. Buradaki amaç, frekans tarağı uygulamaları için yüksek tekrarlama frekanslarında çalışan osilatörler yapmaktır. Deneylerde, %7 Cr:LiCAF kristalinin kullanıldığı x-kavite, 1-W gücünde yüksek parlaklıktaki daralan kılavuz tapılı diyot ile 675 nm de pompalanmıştır. 915 mW güç ile uyarılan Cr:LiCAF lazeri ortalama gücü 51 mW olan, 120 MHz tekrar frekansında, 340 fs genişliğinde darbeler üretmiştir. Rezonatörün sürekli kip-kilitliliğini sağlamak için doyabilen (saturable) Bragg yansıtıcı aynalar kullanılmıştır. Bu çalışmanın ilerleyen aşamalarında, GHz tekrarlama frekanslarına ulaşılması beklenmektedir.

Tezin ikinci kısımında 776 nm dalga boylarında femto-saniye atımlar üreten 5.53MHz tekrarlama frekansına sahip, çok yansımalı Ti:Safir (MPC-Ti:A_2O_3) laseri ile fotoiletken anten kullanarak THz radyasyonu üretmek amaçlanmıştır. Ortalama gücü 60-70mW olan 98fs lik Ti:safir lazerinin çıkışı LtGaAs yapılı fotoiletken anten üzerine odaklanarak 5mV genlikli 0.1-0.7 THz bant genişliğine sahip THz atımı ölçülmüştür. Daha iyi anten ve algılama düzenegi kullanarak, daha geniş bant genişliğine sahip ve daha yüksek verimlilikte THz üretimini amaçlamaktayız.

ACKNOWLEDGMENTS

I would like to express my gratitude to my supervisor Prof. Dr. Alphan Sennaroğlu for giving the opportunity of working in this beautiful laboratory and for his invaluable guidence in the supervision of the thesis.

I would like to thank Asst. Prof. Dr. Ümit Demirbaş for his helpful guidence and Ersen Beyatlı for his collaboration in the Cr:LiCAF experiments.I would also like to thank Dr. Devrim Köseoğlu for the Terahertz part of this thesis.

I also wish to thank Asst. Prof. Dr. Şükrü Ekin Kocabaş for accepting to evaluate my thesis as a jury member.

I would like to thank Adnan Kurt, Associate Prof. Dr. Sarper Özharar, Natali Cizmeciyan, Işınsu Baylam, Ferda Canbaz, İsmail Yorulmaz, Philipp Heck Mustafa Eryürek,Refik Ergün,Cem Yetişmişoğlu, Merve Şahin for their support and friendship during the preparation of this thesis.

Finally, my special thanks and gratitude go to my parents Sultan Cihan, Şeref Cihan, and my sister Canan Cihan who have always encouraged me both emotionally and intellectually during my life.

Table of Contents

List of Tables

List of Figures

Nomenclature

$A_{eff,L}$: the effective laser mode area inside the gain medium on the SBR

c: speed of light in vacuum

d: distance

d_g: length of the gain medium

D_v: group delay dispersion parameter

E: energy level

E_A: the saturation energy of the saturable absorber

E_{gap}: band-gap energy

E_{sat}: saturation energy

f: focal length

f_{rep}: repetition rate of the pulses

$F_{sat,A}$: the absorption saturation fluence of the SBR

g: ground state energy level

$g(v)$: lineshape function

G: gain

G_0: small-signal fractional gain

h: Planck's constant

I : the intensity of the electromagnetic wave

l_e: the effective length of the dipole antenna

I_p: pump intensity

I_{sat}: saturation intensity

$J(t)$: the current in the dipole

k: wave vector

L_c: cavity length

L_{eff}: effective optical path length

m: the effective mass of the carrier.

M_T: transformation matrix

n: refractive index

n_0: low intensity refractive index

n_2: nonlinear refractive index

N_g: ground state population

γ_0: small-signal gain coefficient

ε_0: permittivity of free space

η: slope efficiency

θ_i: incident angle

λ_L: laser wavelength

λ_p: pump wavelength

Δv: bandwidth

v_L: laser frequency

v_p: phase velocity

v_g: group velocity

$v(t)$: velocity of the photocarriers

v_{FSR}: free spectral range

q: q-paramater of the beam

$Q(t)$: the time dependent saturable loss which gives the fractional loss in the propagating power

Q_0: the small signal loss of the absorber

P: power

$P_L(t)$: the instantaneous intracavity laser power

R: reflectivity

ρ: ray vector

σ_a: absorption cross section

σ_e: emission cross section

$\sigma(v)$: transition cross section function

τ_f: fluorescene lifetime

τ_p: pulse width / cavity photon lifetime

T: transmission

ϕ: phase

Ω: solid-angle

ω: angular frequency

$w(z)$: spotsize function

w_0: beam waist

z_0: Rayleigh range

$\otimes$: *the convolution product,*

Dedicated to my parents and my sister Canan

Chapter 1: Theoretical Background on Lasers and Laser Mode Locking

1.1 Introduction and Overview of the Thesis

Mode-locked lasers are very crucial tools for a variety of applications in many areas of science and technology such as biomedical imaging, precision material processing, high harmonic generation and spectroscopy [1-5]. This is because, they emit a periodic train of ultrashort pulses with high peak powers, making them suitable for studying nonlinear interactions in different media. Furthermore, femtosecond pulses typically have high peak powers at low average powers, hence reducing the unwanted effects of thermal heating in the materials. When viewed in the frequency domain, the mode-locked laser spectrum consists of a series of equally spaced modes collectively called a "frequency comb" . In recent years, frequency combs have been successfully utilized in metrology to make precise frequency measurements.[6] Hence, there is a great deal of interest for developing low-cost, robust, compact and efficient femtosecond lasers for time and frequency domain applications. Furthermore, higher repetition rates are advantageous in many applications because of higher power per mode which increases the signal-to-noise ratio in measurements.

The experimental work in this thesis is divided into two major parts. In the first part, a highly efficient, diode pumped Cr:LiCAF laser was designed and constructed. By employing a 1-W tapered diode pump, efficient continuous wave and mode locked operation were successfully demonstrated. In order to initiate the mode-locked operation, a semiconductor Bragg reflector mirror (SBR) was added into the cavity. By using 915 mW of pump power, the Cr:LiCAF laser produced 340 fs pulses around 800 nm with an output

power of 51 mW at a repetition rate of 120 MHz. The availability of high power diode pump sources is expected to increase the output power of the laser and make it possible to obtain high repetition rates up to or beyond 1 GHz. Such a source will have a significantly high power per mode and should find applications in measurements requiring high signal to noise ratio.

The second part of the thesis work utilizes a home-built multi-pass cavity femtosecond Ti:Sapphire laser, generating 98 fs pulses with a repetition rate of 5.53 MHz at 776 nm, to obtain THz radiation from a photoconductive antenna. We used a photoconductive antenna(PCA) made of low-temperature grown gallium arsenide (Lt-GaAs) . The detection of the THz waves was further accomplished with a second PCA. The generated THz waves which had a signal strength of 5 mV were in the frequency range of 0.1-0.7 THz. With improved antenna and detection design, we expect to further improve the bandwidth and efficiency of the THz generation

In Chapter 1, starting from Section 1.2, we present some background about geometical optics, where we neglect the wave aspects of light and introduce a useful matrix formalism for the analysis of complex optical systems in the paraxial approximation regime. Matrix formalism is then applied to the analysis of the multipass-cavity and useful results are outlined. We then discuss four level atomic systems where the rate equationapproach is developed and solved to analyze steady-state laser operation. Q-switching condition with a saturable absorber is also investigated. Furthermore, we give a concise review of some important nonlinear interactions such as Kerr lens mode locking, group delay dispersion and self phase modulation. Chapter 1 plays a critical role in the understanding of the key concepts used in the experimental parts of this thesis. Chapter 2 is devoted to the detailed design and construction of the Cr:LiCAF laser which can be made to work at repetitin rates above 100 MHz. Here, the components playing a key role in the design of the highly efficient Cr:LiCAF laser such as tapered diodes and the semiconductor Bragg mirrors are investigated in detail and the experimental parameters are presented. Chapter3 starts with a brief historical review of milestones in THz science. Then, THz wave generation and detection methods are discussed. Also, the characteristic components in our THz setup such as the interdigitated photoconductive antenna (ICPA) and the 90 degree parabolic mirrors are presented.The

multipass-cavity Ti:Sapphire laser driven THz generation system using a photoconductive antenna is described and the obtained results are discussed.

1.2 Matrix Methods in Paraxial Optics

In this part, we describe how matrices can be used to describe an optical system in which all optical elements are centered on the same optical axis. For the validity of of our results, we need two main approximations[7].

The first approximation is that wavelength of light is negligibly small so that its propagation cannot be described in terms of the wavefronts but in terms of rays. The second approximation is that only the paraxial rays that remain close to and almost paralel to the optical axis will be considered. Thus, the sine or tangent of any angle will be approximated as the the angle itself working in radian units. The methodology will not reveal the higher-order effects such as aberrations, astigmatism, and distortion.

If we consider the propagation of a paraxial ray through an optical system of centered components, generally two parameters will be required to describe the ray of light: its height r and slope θ with respect to the optical axis. Therefore, this ray is described as 2x1 column vector. An optical system will modify these ray parameters so that the emerging ray at the output plane will have a different height r_2 and a different slope θ_2 as shown in Fig.1.1.

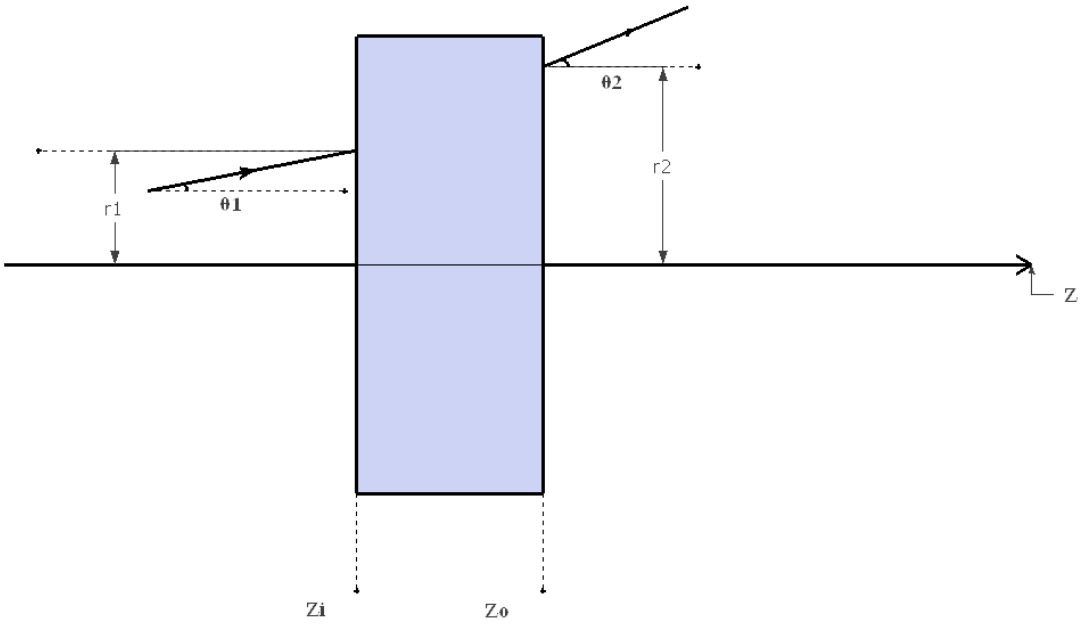

Figure 1. 1 *Sketch of a general paraxial optical system. (Adopted from [8])*

The relation between the output ray and the input ray can be formulated as

$$\vec{r}_f = \mathbf{M_T}\vec{r}_i \quad , \tag{1.1}$$

where the final ray vector $\vec{r}_f$ and the initial ray vector $\vec{r}_i$ are given by

$$\vec{r}_f = \begin{bmatrix} r_f \\ \theta_f \end{bmatrix} \text{ and } \vec{r}_i = \begin{bmatrix} r_i \\ \theta_i \end{bmatrix} \tag{1.2}$$

$\mathbf{M_T}$ in Eqn. (1.1) is the transformation matrix

$$\mathbf{M_T} = \begin{bmatrix} A & B \\ C & D \end{bmatrix} \quad . \tag{1.3}$$

The following explicit expressions are obtained by expanding the ray transformation described by Eq (1.1):

$$r_f = Ar_i + B\theta_i \tag{1.4}$$

$$\theta_f = Cr_i + D\theta_i \tag{1.5}$$

By using the special rays $\vec{\rho}_1$ and $\vec{\rho}_2$, the four elements of the ray transformation matrix $\mathbf{M_T}$ are determined. A more detailed description of this method may be found in Ref. [8]. Each element in a system can be represented by a ray transformation matrix. In order to obtain a single matrix to represent the complete system, we multiply the transformation matrix of each optical element in the correct sequence:

$$\mathbf{M_T} = \mathbf{M_{Tn}}\mathbf{M_{Tn-1}} \dots \mathbf{M_{T1}} = \prod_{\mathbf{i=n}}^{\mathbf{1}} \mathbf{M_{Ti}} \tag{1.6}$$

The parameter $q(z)$ is the q-parameter of the beam and it includes information about the radius of curvature $R(z)$ and the spot size function $w(z)$of the beam. Q(z) can be calculated by using the equation

$$\frac{1}{q(z)} = \frac{1}{R(z)} - i\frac{\lambda}{n_0 \pi w^2(z)} \tag{1.7}$$

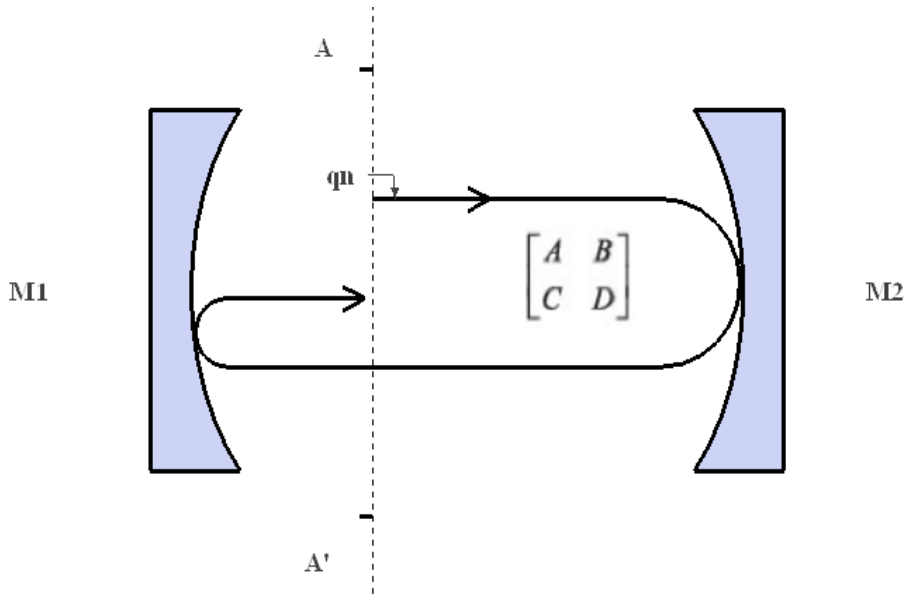

Figure 1. 2 *A general paraxial resonator, where q_n and q_(n+1) represent the q-parameters of the self consistent Gaussian beam at the plane AA' after n and (n+1) round trips. (Adopted from [8])*

If the laser beam returns to its initial plane AA' in *Fig.1.2,* the determinant of the transfer matrix will be unity. Further, if q_n *and* q_{n+1} represent the q parameters of the self consistent Gaussian beam after n and (n+1) round trips, a self-consistent Gaussian beam should satisfy

$$q_n = q_{n+1}. \tag{1.8}$$

By using the transformation rule fort he q parameter of a Gaussian beam, q_n and q_{n+1} are further related through

$$q_{n+1} = \frac{Aq_n+B}{Cq_n+D} \tag{1.9}$$

1.3 Multipass Cavities

The multipass cavity (MPC) was first introduced by Herriot et all in 1964 [9] to provide a long effective optical path with a compact arrangement of optics.Let us describe the MPC in its simplest version where we have two highly reflecting mirrors and notches for beam injection and extraction. This is shown in Fig.1.3. When the seperation and the radii of the mirrors are properly chosen, an incident beam with the correct offset and tilt with respect to the optical axis will bounce many times between the end mirrors before exiting through the second notch. In this section, we will analyze the optical characteristics of MPCs by using the ray and beam analysis methods developed for paraxial optical systems.

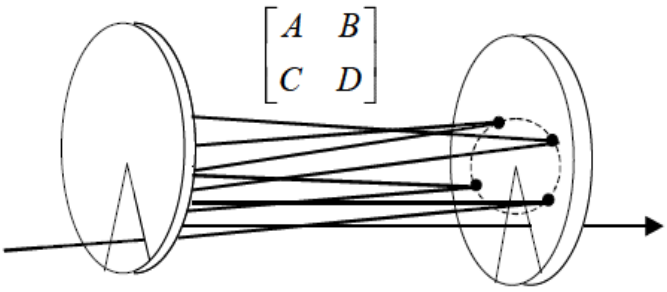

Figure 1. 3 *A schematic of a general multi-pass cavity. One round trip is represented by the ABCD matrix.(Taken from[10])*

Assume that a single round trip within the MPC is represented by the ray transformation matrix M_T. If the elements A and D of M_T satisfy the inequality

$$\left|\frac{A+D}{2}\right| \leq 1, \tag{1.9}$$

then the MPC will be stable in the sense that a ray originating near the optical axis will remain close to the optical axis after an indefinite number of roundtrips. Since the bouncing beam returns to the same location after each round trip, the determinant of M_T is further unity. It can be shown that (see Ref. [8]), the ray transformation matrix for n full round trips inside the MPC becomes

$$M_T^n = \begin{bmatrix} \frac{A-D}{2}\frac{sin\, n\emptyset}{sin\emptyset} + cosn\emptyset & B\frac{sinn\emptyset}{sin\emptyset} \\ C\frac{sinn\emptyset}{sin\emptyset} & \frac{D-A}{2}\frac{sin\, n\emptyset}{sin\emptyset} + cosn\emptyset \end{bmatrix} \tag{1.10}$$

We can apply the tranfer matrix of the MPC for an incident light ray $\vec{r_i} = \begin{bmatrix} r_0 \\ \theta_0 \end{bmatrix}$. After n full round trips, the ray vector $\overrightarrow{r_n}$ becomes

$$\overrightarrow{r_n} = M_T^n \overrightarrow{r_n} \tag{1.11}$$

The transverse offsets x_n and y_n of the ray after the nth round trip become

$$x_n = x_0\, cosn\emptyset + \left(\frac{x_0(A-D)+2B\theta_{x0}}{2sin\emptyset}\right) sinn\emptyset \tag{1.12}$$

$$y_n = y_0\, cosn\emptyset + \left(\frac{y_0(A-D)+2B\theta_{y0}}{2sin\emptyset}\right) sinn\emptyset \tag{1.13}$$

Under special conditions, these ellipses described by the spot pattern may become circular. If we consider the case where the initial ray parameters are chosen according to

$$y_0 = 0\ ,\ \theta_{y0} = \frac{x_0 sin\emptyset}{B}, \theta_{x0} = \frac{x_0}{2B}(D - A) \quad , \tag{1.14}$$

then, the coordinates of the bouncing spots become

$$x_n = x_0 cosn\emptyset \ \ y_n = x_0 sinn\emptyset \quad . \tag{1.15}$$

The resulting spot pattern is shown in Fig.1.4 for an actual multipass cavity constructed in our laboratory.

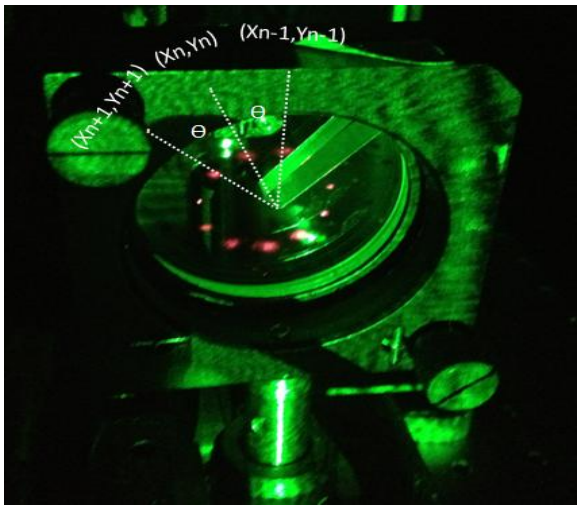

Figure 1. 4 *A circular spot pattern is obtained at the input reference plane of a multi-pass cavity when the position and tilt of the incident ray is adjusted according to Eq. 1.14.*

When the laser is mode locked, the pulse repetition rate is given by

$$f_{rep} = \frac{c}{2d} \quad , \tag{1.16}$$

Where c is the speed of light and d is the total length of the cavity.

Then, the energy per pulse can be calculated using

$$W_p = \frac{P_{out}}{f_{rep}} . \quad (1.17)$$

Often it is desirable to use q-preserving MPCs in which the exiting beam has the same q-parameter as the input beam. This makes it very easy to add a long MPC to a short cavity without altering the original spotsize distribution. If the laser is mode locked, the output pulse energy is directly proportional to the cavity length as can be seen from Eqns(1.16-1.17). For a detailed analysis of q-preserving MPCs refer to Refs. [10-12]

1.4 The Lineshape Function

We now turn our attention to light-matter interactions. The function $\sigma(v)$ centered about the resonance frequency v_0 , of an atomic transition, characterizes the interaction of the atom with the radiation field and is called transition cross section (see Fig.1.5a). It has the dimensions of cm^2 . The area S under the transition cross section function represents the strength of the interaction and has the units of $cm^2 - Hz$ [13]. S is given by

$$S = \int_0^\infty \sigma(v)dv \quad (1.18)$$

By normalizing the transition cross section function, we obtain the lineshape function $g(v) = \frac{\sigma(v)}{S}$ which has the units of Hz^{-1} and a unity area. Thus, the transition cross section $\sigma(v)$ can be conveniently expressed as

$$\sigma(v) = Sg(v) \ . \quad (1.19)$$

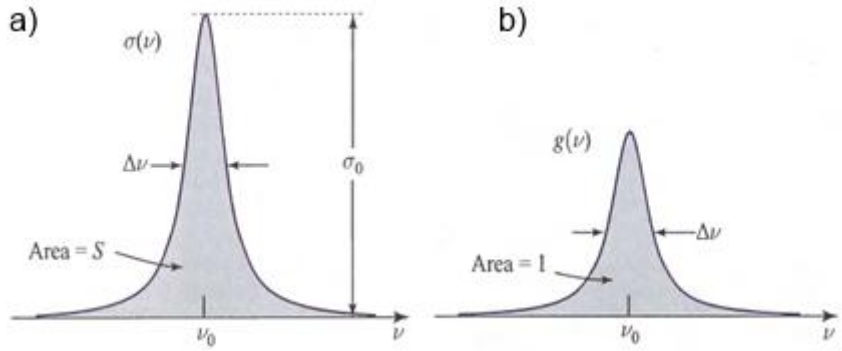

Figure 1. 5 *a)The transition cross section σ(ν) and b)the lineshape function g(ν).(taken from[13])*

The lineshape function $g(v)$ is centered about the resonance frequency v_0 as can be seen in Fig.1.5b.Transitions are therefore most likely for photons of frequency $v \approx v_0$. The width of the function $g(v)$ is known as the transition linewidth. The linewidth Δv is usually defined as the FWHM of the function $g(v)$.

1.5 Four-Level Atomic Systems

In this section, the rate equation formulation will be developed and solved to analyze steady-state laser operation in simplified four-level laser systems. Obtaining population inversion and low threshold laser operation is more feasible in four-level atomic systems than in three-level and two-level atomic systems. A schematic of an ideal four level system is shown below.

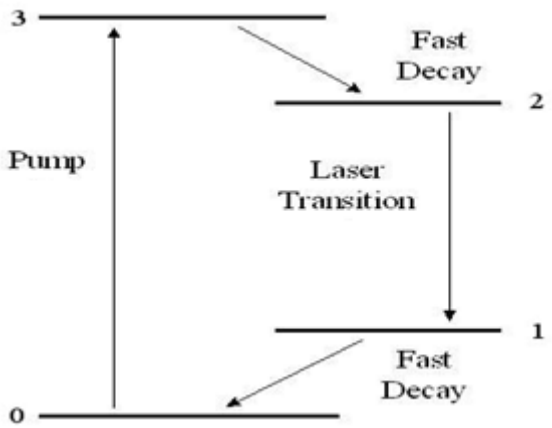

Figure 1. 6 *Energy level diagram of an ideal four-level atomic system.*

Here, we will describe the mechanism of an idealized four level atomic system and obtain the rate equation. As shown in Figure 1.6, a pumping mechanism first raises the atoms from the ground state $|0\rangle$ to the pump band $|3\rangle$. For an ideal four level system, the decay rates from the pump band to the upper level $|2\rangle$, and from the lower level $|1\rangle$ to the ground state are much faster than the decay rate from level $|2\rangle$ to level $|1\rangle$. As a result, we can neglect the populations in levels $|3\rangle$ and $|1\rangle (N_3 = N_1 \sim 0)$. Based on these assumptions, the rate equation for the population density of level $|2\rangle$ becomes

$$\frac{dN_2}{dt} = W_p N_g - \sigma \frac{I}{h\nu}(N_2 - N_1) - \frac{N_2}{\tau_f} \tag{1.20}$$

where the parameters are defined as follows:

N_g= ground state population,

I = the intensity of the electromagnetic wave which is nearly resonant with the transition,

h = the Planck's constant,

τ_f=fluorescence lifetime of the upper state,

N_2 = the population density of the level 2.

Further, the total atomic density N_t, can be expressed as the sum of the total atomic densities of the ground state and the upper level since the atoms are either in the ground state $|0\rangle$ or the upper level $|2\rangle$. In equation form, we have

$$N_2 + N_g = N_t \quad . \tag{1.21}$$

The steady state population inversion is given by

$$\Delta N = \frac{\Delta N_0}{1+\frac{I}{I_s}} \quad , \tag{1.22}$$

where ΔN_0 and I_s are defined as

$$\Delta N_0 = \frac{N_t W_p \tau_f}{1+W_p \tau_f} \textit{ (the small-signal inversion),} \tag{1.23}$$

and

$$I_s = \frac{h\nu}{\sigma \tau_f}(1 + W_p \tau_f) \textit{ (the saturation intensity).} \tag{1.2}$$

The rate-equation analysis shows that an ideal four-level atomic system always has population inversion in the presence of pumping which is characterized by the pumping rate $|W_p|$. However, to obtain net amplification, $|W_p|$ should be above a certain threshold value to overcome other resonator losses as will be investigated in the following analysis.

We consider the simplest resonator configuration that consists of only two mirrors and define the parameters such that $R_1$and R_2 are the intensity reflection coefficients of the mirrors, γ_0 is the small signal differential gain coefficient,and α_L represents all sources of loss inside the gain medium whose length is denoted as d_g.Thus, the net small-signal gain will be $\gamma_0 - \alpha_L$, and the intensities at some point inside tha cavity after the m_{th} and $(m+1)_{th}$ round trips will be denoted as I_m and I_{m+1} . Then, the intensities of the beam circulating inside the cavity after two consecutive round trips can be expressed as

$$I_{m+1}=I_m R_1 R_2 \exp\left(2d_g(\gamma_0 - \alpha_L)\right) . \quad (1.25)$$

At the oscillation threshold, when the gain is just large enough to oversome the losses, we can say that $I_{m+1}=I_m$ and obtain

$$(\gamma_0)_{th} = \alpha_L + \frac{1}{2d_g}\ln\left[\frac{1}{R_1 R_2}\right] \quad . \quad (1.26)$$

The corresponding population inversion at threshold becomes

$$\Delta N_0 = \frac{(\gamma_0)_{th}}{\sigma_e} \quad . \quad (1.27)$$

The threshold inversion in Eq. (1.27) can be written by using the result (1.26). Afterwards, the threshold pumping rate $(W_p)_{th}$ to achieve this population inversion can be calculated by using Eq. (1.23).

1.6 Passive Q-Switching with Saturable Absorbers

In contrast to active Q-switching where the timing and duration of the change in the quality factor Q are under active external control, when a saturable absorber is placed inside the laser cavity, the laser can generate a pulsed output. This is called passive Q-switching. Saturable absorbers(such as semiconductor saturable absorbers known as SESAMs or saturable Bragg

reflectors known as SBR) [14, 15] introduce large losses at low light intensities and low level of losses at high light intensities which causes the high intensity pulses to experience relatively lower loss than low intensity pulses. That results in the generation of repetitively Q-switched pulses. References [16, 17] will be a basis for our brief outline of passive Q-switching. The following equation describes the saturable loss

$$\frac{dQ}{dt} = -\frac{Q(t)-Q_0}{\tau_A} - \frac{Q(t)P_L(t)}{E_A} \quad , \tag{1.28}$$

where:

$Q(t)$ is the time dependent saturable loss which gives the fractional loss in the propagating power,

τ_A is the decay time of the absorber atoms,

Q_0 is the small signal loss of the absorber,

$P_L(t)$ is the instantaneous intracavity laser power,

E_A is the saturation energy of the saturable absorber given by,

$$E_A = \frac{h\nu_L}{\sigma_a} a_{abs} \quad . \tag{1.29}$$

In Eq. (1.29),

a_{abs} is the effective beam area in the saturable absorber,

σ_a is the absorption cross section of the saturable absorber.

Under the assumptions that the transfer relaxation times for the gain medium and the saturable absorber are much faster than any other dynamics in our system and that the change in gain, intensity, and saturable absorption is small compared to the round trip time in the cavity, the laser rate equations can be expressed as:

$$\frac{dG}{dt} = -\frac{G(t)-G_0}{\tau_f} - \frac{G(t)P_L(t)}{E_{sat}} \tag{1.30}$$

$$\frac{dP_L}{dt} = -\frac{2}{T_R} - \big(\, G(t) - l - Q(t)\big)P_L(t) \tag{1.31}$$

Above, l is the single-pass, non-saturable, fractional power loss and can be expressed as (see Eq. 1.25)

$$l = \frac{2\alpha_L d_g + \ln\left(\frac{1}{R_1 R_2}\right)}{2} \quad . \tag{1.32}$$

A linearized stability analysis of Eqs. (1.30) and (1.31) gives the stability criterion against Q-switching of a cw running laser.

$$-2P\,\frac{dQ}{dP_L}\Big|_{cw} < \frac{r}{T_f}\Big|_{cw} \; with \; r = 1 + \frac{P}{P_{sat}} \; and \; P_{sat} = \frac{E_{sat}}{\tau_f} \tag{1.33}$$

where r is the pump parameter that describes at how many times above the threshold the laser operates,

The physical meaning of the inequality (1.33) can be explained in a simple approach. The right side of (1.33) is the relaxation to equilibrium for the gain at a given pump power and constant laser power. The left side is the decay time of a power fluctuation of the laser at a fixed gain. If the gain cannot react fast enough to fluctuations of the laser power, relaxation oscillations grow and result in passive Q-switching of the laser. In addition,

$$-2T_L P_L\,\frac{dQ}{dP_L}\Big|_{cw} = 2T_L Q_0\,\frac{P/\chi P_{sat}}{(1+\frac{P_L}{\chi P_{sat}})^2} < r|_{cw} with \;\; \chi = \frac{P_A}{P_{sat}} \quad . \tag{1.34}$$

As can be inferred from Eq.(1.34), repetitive Q-switching will be obtained when the following condition is satisfied:

$$-2T_L P_L \frac{dQ}{dP_L}\Big|_{cw} = \frac{2q_0 T_f}{\chi} > 1 \tag{1.35}$$

where:

$$\chi = \frac{P_A}{P_{sat}} \tag{1.36}$$

Further, the frequency f_{rep} of the pulse train is given by

$$f_{rep} = \frac{1}{\tau_f}\frac{G_0}{2Q_0} \quad . \tag{1.37}$$

The result in Eq.of (1.37) shows that, as the pump power increases, the small signal gain G_0 gets larger and the pulse repetion rate increase

1.7 Mode Locking of Lasers

Another regime of pulse laser operation involves the oscillation of the cavity modes with a constant phase to produce pulses with duration shorter than the cavity round trip time. In this section, the concept of mode locking which is used in generating pulse durations in the picsecond, femtosecond, and more recently attosecond ($x10^{-18}sec$) time scales will be overviewed.[18]

Lasers can oscillate on many longitudinal modes with frequencies that are equally separated by the Fabry-Perot intermodal spacing. Although these modes normally oscillate independently, it is possible to couple them and lock their phases together. Here, we consider the interference of M monochromatic waves with equal intensities and equally spaced

frequencies in order to explain the mode locking phenomenon. Let us suppose that the spatial distribution of the mode is TEM_{00}.The resonator can support infinitely many longitudinal modes at discrete frequencies given by

$$v_q = q\frac{c}{2d} \tag{1.38}$$

where:

q is an integer,

c is speed of light in vacuum,

d is the effective optical length of the resonator.

The free spectral range v_{FSR} is the frequency spacing between two adjacent modes and is given by

$$v_{FSR} = v_{q+1} - v_q = \frac{c}{2d} \tag{1.39}$$

The total complex wavefunction of the field can be expressed as a sum in the form

$$E(t) = \sum_{q=0}^{M-1} E_q \exp\left(j(w_0 + qw_F)t + j\varphi_q(t)\right) \tag{1.40}$$

The mode locking which is a regime of a periodic train of ultrashort optical pulses, can be achieved by operating the modulator in such a way as to force all modes to oscillate with a constant phase. When the phase factors are set to zero and the same amplitude assumed for each mode, we obtain

$$E(t) = \sum_{q=0}^{M-1} E_q \exp\left(j(w_0 + qw_F)t\right) = E_0 \exp\left(jw_0 t\right)\frac{1-\exp\left(jMw_F t\right)}{1-\exp\left(jw_F t\right)} \tag{1.41}$$

$$= E_0 \exp\left(jw_0 t\right)\frac{\sin\left(\frac{Mw_F t}{2}\right)}{\sin\left(\frac{w_F t}{2}\right)} \tag{1.42}$$

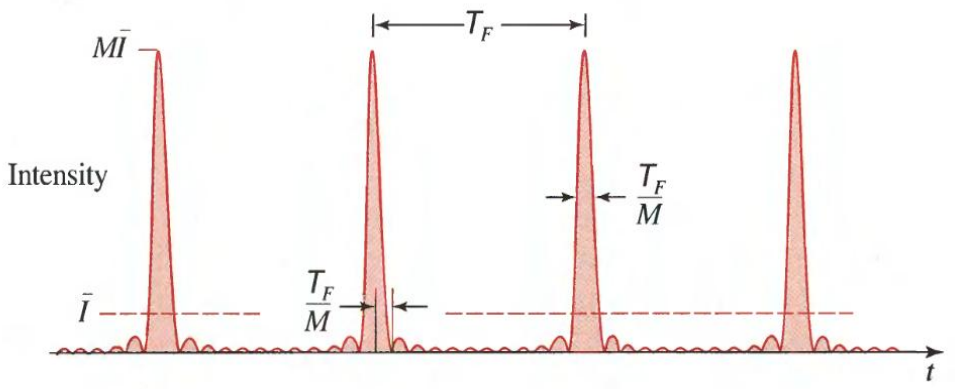

Figure 1. 7 *Intensity of the periodic pulse train resulting from the sum of M laser modes of equal magnitude and phase. Each pulse has a duration M times smaller than the period T_F and a peak intensity M times greater than the mean intensity.(taken from [13])*

As shown in Fig.1.7, the average power is proportional to $Mx|E_0|^2$, the peak power of the pulses is M times larger than the average power. In other words, as the number of locked modes increases, the corresponding peak power of the mode locked laser becomes larger. If we roughly define the pulse width τ_p, as the time difference between the pulse peak and the first zero the following formulas can be used to estimate the pulse width:

$$\frac{Mw_F\tau_p}{2} = \pi \tag{1.43}$$

$$\tau_p = \frac{1}{M}\left(\frac{2\pi}{w_F}\right) = \frac{T_R}{M} \tag{1.44}$$

The formula above shows that as the number of locked modes increases, the pulse width decreases as depicted in Fig.1.7. Furthermore, since the number of locked modes Mcan be estimated from $M \approx \frac{\Delta v}{v_{FSR}}$, we arrive at the result $\tau_{\text{pulse}} = \frac{T_F}{M} \approx \frac{1}{\Delta v}$. The pulse duration τ_{pulse} is therefore inversely proportional to the atomic linewidth Δv. In tunable solid-state

lasers such as Ti:sapphire and Cr:LiCAF, Δv can be quite large, of the order of several THz, leading to the generation of very short pulses in the femtosecond range.

1.8 Group Delay Dispersion (GDD)

In a dispersive medium, the susceptibility $x(v)$, electric permittivity $\epsilon(v)$, refractive index $n(v)$, and the phase/group velocities are all functions of frequency.

Assume that the initial complex wavefunction at z=0 is given by

$$U(0,t) = A(t)\exp\,[jw_0 t] \tag{1.45}$$

where:

w_0 *is the central angular frequency and*

$A(t)$ *is the complex envelope of the wave*

If n varies slowly, the complex wavefunction at a distance z can be approximated

$$U(z,t) = A(t - \frac{z}{v_g})\exp\,[jw_0\left(t - \frac{z}{c}\right)] \tag{1.46}$$

$c = c_0/n(w_0)$ is the speed of light in the medium at the central frequency, and v_g is the velocity at which the envelope travels and is given by

$$v_g = \frac{dw}{dk} \quad . \tag{1.47}$$

Here:

$k = \frac{wn(w)}{c_0}$ is the frequency-dependent propagation constant.

The corresponding time delay $\tau_d = \frac{z}{v_g}$ is called the group delay. Since the phase factor exp $[jw_0\left(t - \frac{z}{c}\right)]$ is a function of $t - \frac{z}{c}$. The speed of light c is the phase velocity here, and it is given by

$$v_p = \frac{w}{k} \tag{1.48}$$

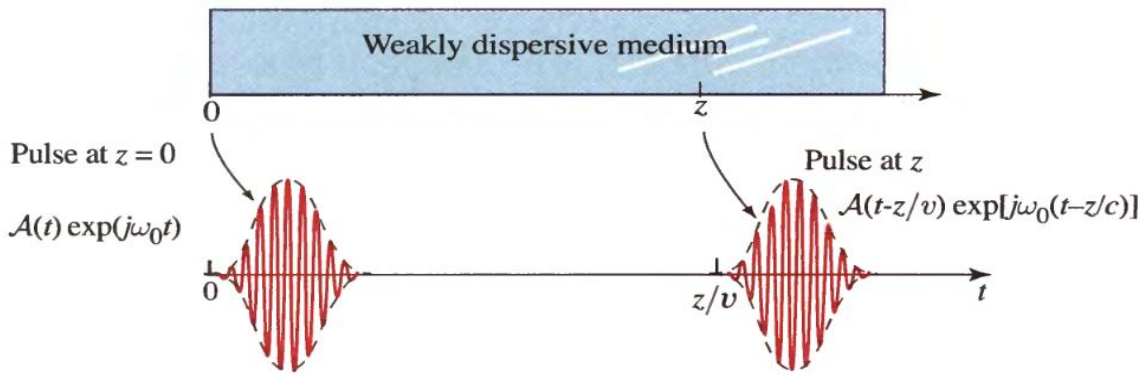

Figure 1. 8 *An optical pulse traveling in a dispersive medium that is weak enough so that its group velocity is frequency independent. The envelope travels with group velocity v_g while the underlying wave travels with phase velocity c.(taken from[13])*

Since the group velocity $v_g = \frac{dw}{dk}$ is itself often frequency dependent, different frequency components of the pulse undergo different delays $\tau_d = \frac{z}{v_g}$. As a result, the pulse spreads in time. This phenomenon is known as group delay dispersion (GDD). If we consider two identical pulses of central frequencies v and $v + \delta v$, upon traveling a distance z, they suffer a differential group delay

$$\delta_\tau = \frac{d\tau_d}{dv}\delta v = \frac{d}{dv}\left(\frac{z}{v}\right)\delta v = D_v z \delta v \tag{1.49}$$

where:

$$D_v = \frac{d}{dv}\left(\frac{1}{v_g}\right) = \frac{d^2k}{dw^2} \quad (1.50)$$

is called the dispersion coefficient or the group delay dispersion (GDD) parameter.

If $D_v > 0$, the medium is said to exhibit normal dispersion. In this case, the the long-wavelength components of an optical pulse propagate faster than the short-wavelength components.
If $D_v < 0$ the medium is said to exhibit anomalous dispersion, this time the shorter wavelength components travel faster and arrive earlier.

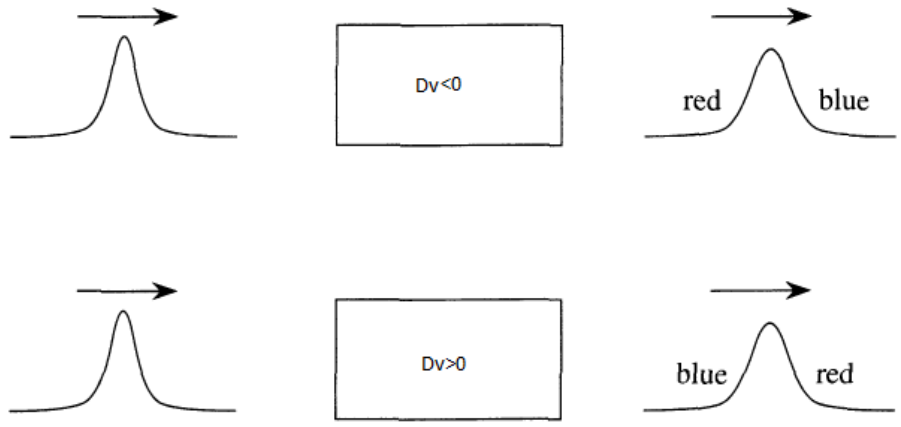

Figure 1. 9 *Propagation of an optical pulse through media with normal and anomalous dispersion. (taken from [19])*

The electric field of the pulse propagating in the nonlinear and dispersive medium along the z axis can be written as

$$\mathrm{E(z,t)} = \mathrm{e}^{\mathrm{j(w_0 t - k_0 z)}} \int_{-\infty}^{\infty} \mathrm{S(w_0 + \Omega) e}^{\mathrm{j(\Omega t - k'\Omega\, z - k''\Omega^2\, z/2)}}\, \mathrm{d\Omega} \tag{1.51}$$

where:

$S(w)$ is the Fourier spectrum of the pulse,

$k(w) = k_0 + k'(w - w_0) + \frac{1}{2}k''(w - w_0)^2 + \cdots$ is the propagation constant in dispersive medium, and

Ω is the frequency measured from the reference frequency w_0.

Then the amplitude (or the envelope function) of the pulse can be written as

$$A(z,t) = \int_{-\infty}^{\infty} S(w_0 + \Omega) e^{j(\Omega t - k'\Omega\, z - k''\Omega^2\, z/2)}\, d\Omega \tag{1.52}$$

Taking partial derivatives in Equation (1.52), we can derive a differential equation for the propagation of the amplitude and we obtain the envelope wave equation for $\mathrm{A(z,t)}$ in dispersive media as follows:

$$\frac{\partial \mathrm{A}}{\partial \mathrm{z}} + \frac{1}{\mathrm{v_g}}\frac{\partial \mathrm{A}}{\partial \mathrm{t}} - \mathrm{j}\frac{\mathrm{k''}}{2}\frac{\partial^2 \mathrm{A}}{\partial \mathrm{t}^2} = 0 \tag{1.53}$$

After the addition of the correction term into the propagation constant due to the Kerr effect, Eqn.(1.52) becomes

$$\mathrm{A(z,t)} = \int_{-\infty}^{\infty} \mathrm{S(w_0 + \Omega) e}^{\mathrm{j(\Omega t - k'\Omega\, z - k''\Omega^2\, z/2)}}\, \mathrm{e}^{\mathrm{jk_2 Iz}} \mathrm{d\Omega} \tag{1.54}$$

where:

$I = \frac{1}{2}\varepsilon_0 n_0 |A(z,t)|^2$ is the local intensity of the wave,

$k_2 = \frac{w_0}{c} n_0$.

After taking the spatial derivative of amplitude in Eqn.(1.54), and applying a transformation $\tau = t - \frac{z}{v_g}$,the equation for the field amplitude including the Kerr effect becomes

$$-\frac{\partial A}{\partial z} - j\frac{k''}{2}\frac{\partial^2 A}{\partial \tau^2} = -\frac{1}{2}w_0\varepsilon_0 n_0 n_2 |A|^2 A \tag{1.55}$$

Equation (1.55) is known as the nonlinear Schrodinger equation. This equation governs the propagation of the optical pulse in a nonlinear dispersive medium. Note that the second term on the left-hand side and the term on the right-hand side show the distortions (temporal or spectral broadening) that the pulses experience. For a further discussion of the nonlinear Schrodinger equation refer to [13, 19-21]

1.9 Kerr Lens Mode Locking and Self Phase Modulation

The Kerr effect was first reported in 1875 [22]. A nonlinear dielectric medium is characterized by a nonlinear relation between the polarization density P and the electric field $\mathcal{E}$ according to [13]

$$P = \epsilon_0 \chi \mathcal{E} + 2d\mathcal{E}^2 + 4\chi^3 \mathcal{E}^3 + \cdots, \quad . \tag{1.56}$$

The second term and the third term in Eqn.1.56 represent second-order and third-order nonlinearities, respectively. In centrosymmetric medium, the second-order nonlinear term is absent and the polarization reverse exactly when the electric field is reversed. In such a case,

$$P_{NL} = 4\chi^3 \mathcal{E}^3 \tag{1.57}$$

the nonlinearity is dominated by the third order term and the material is called a Kerr medium. Kerr media generates third harmonic, sums and differences of triplets of frequencies in the response of the optical fields If a monochromatic optical field $\mathcal{E}(t) = Re\{E(w)\exp(jwt)\}$ is applied to the third-order nonlinear medium, a nonlinear polarization $P_{NL}(t)$ that contains components at frequency w and $3w$ is created.

$$P_{NL}(w) = 3\chi^3|E(w)|^2E(w) \tag{1.58}$$

$$P_{NL}(3w) = \chi^3E^3(w) \tag{1.59}$$

The change of the susceptibility $\Delta\chi$ can be expressed as follows using Eqn.1.58.

$$\epsilon_0\Delta\chi = \frac{P_{NL}(w)}{E(w)} = 3\chi^3|E(w)|^2 = 6\chi^3\eta I \tag{1.60}$$

where $I = |E(w)|^2/2\eta$ is the optical intensity of the initial wave.

We obtain $2n\Delta n = \Delta\chi$, by differentiating $n^2 = 1 + \chi$. Then, $\Delta n = \frac{3\eta}{\epsilon_0 n}\chi^3 I = n_2 I$,the relation of change in the refractive index proportional to the optical intensity is obtained.

$$n(I) = n + n_2 I \quad . \tag{1.61}$$

This quadratic variation of the refractive index change with field is known as the optical Kerr effect. The duration of the mode locked pulse is limited by the recovery time of the fast saturable absorber in passive mode locking[23]. By using the Kerr lens effect, it is possible to obtain much shorter pulses since the phenomenon is based on the nonlinear refractive index that arises from distortions of the atom's electron cloud. An aperture is placed inside the cavity which blocks the low intensity beam (occupying a larger transverse cross

section) and prevents the lasing. At high intensity, self focusing occurs, the divergence of the beam decreases and the amount of light getting through the aperture increases. Using this method, femtosecond pulses have been generated in many different kinds of tunable solid-state lasers[24-28].

An intensity dependent refractive index has important consequences for the propagation of light through a material. The propagation constant now varies with intensity according to

$$k = \frac{nw}{c} = \frac{n_0 w}{c} + \frac{n_2 I w}{c} = k_0 + \Delta k \tag{1.62}$$

In Eqn.(1.62), k_0 is the low intensity value and Δk is the change in k at high intensity. When the light propagates a distance L in the material, the intensity causes the phase to shift by

$$\Delta\varphi = \Delta k L = \frac{n_2 I w}{c} L \tag{1.63}$$

This intensity dependent shift of phase in Eqn.(1.63) is termed self-phase modulation.

1.10 Temporal and Spectral Widths

The temporal and spectral widths of a pulse are the widths of the temporal intensity $I(t) = |U(t)|^2$ and the spectral intensity $S(v) = |V(v)|^2$. Here, the FWHM will be used and the temporal and spectral widths will be denoted as τ_{FWHM} and Δv respectively. Because of the Fourier transform relation between $U(t)$ and $V(v)$, the spectral width is inversely proportional to the temporal width. The coefficient of proportionality depends on the pulse shape and the definition of width. In this section only the transform-limited Gaussian pulse that can be formulated as in Eqn.(1.64) will be discussed briefly. The amplitude of a Gaussian pulse can be written as

$$A(t) = A_0 \exp\left(-\frac{t^2}{\tau^2}\right) \quad , \tag{1.64}$$

where τ is a real time constant. The intensity, given below by Eq. (1.65), is also a Gaussian function with peak value $I_0 = |A_0|^2$:

$$I(t) = I_0 \exp\left(-\frac{2t^2}{\tau^2}\right) \quad . \tag{1.65}$$

The FWHM is further given by

$$\tau_{FWHM} = \sqrt{2\ln(2)}\tau = 1.18\tau \quad . \tag{1.66}$$

The Fourier transform of the complex envelope and its spectral intensity is a Gaussian function as seen in Eqns.(1.67,1.68).

$$A(v) \sim \exp\left(-\pi^2\tau^2 v^2\right) \tag{1.67}$$

$$S(v) \sim \exp[-2\pi^2\tau^2(v - v_0)^2] \tag{1.68}$$

The FWHM of the spectral intensity is

$$\Delta v = 0.375\tau = 0.44/\tau_{FWHM} \tag{1.69}$$

Then, the product of the FWHM temporal and spectral widths is

$$\tau_{FWHM}\,\Delta v = 0.44 \tag{1.70}$$

Different pulse profiles have different time-bandwidth products. For example, the time-bandwidth product for a chirp-free sech^2 pulse is 0.315.

Chapter 2: Development of a diode-pumped, femtosecond Cr:LiCAF(Cr^{3+}: $LiCaAlF_6$) laser at high repetition rates for optical frequency comb applications

Mode locked lasers emit a train of ultrashort pulses in the time domain with high peak powers. Thiscorresponds to a series of equally spaced frequency spikes called "frequency comb " in the frequency domain. Both of them (time and frequency domain picutres) provied quite usefull tools for many applications. Hence, there is a great deal of interest for developing low-cost, robust, compact and efficient femtosecond lasers for time and frequency domain applications. Furthermore, higher repetition rates are advantageous in many applications because of higher signal-to-noise ratio. Ti:Sapphire has the broadest gain bandwidth among all solid-state laser gain media. However, Ti:Sapphire lasers have high loss[29], high lasing thresholds[30] , and its conventional pump sources (frequency-doubled neodymium and ytterbium lasers) are quite expensive, bulky and electrically inefficient which is an important limiting factor for the widespread usage of Ti:Sapphire technology.

Cr^{3+}-doped colquiriites (Cr:LiSAF, Cr:LiCAF[31], Cr:LiSGaF) can be regarded as promising alternatives to Ti:Sapphire, because of their several favorable laser characteristics including: (i) strong and broad absorption bands around 630 nm which makes wavelength and polarization flexible direct diode pumping possible by low-cost diodes [32, 33] (ii) broad gain bandwidths around 800nm leading to generation of pulses on a 10-fs level, and (iii) near-unity quantum efficiency to allow construction of quite efficient lasers. These properties enable construction of compact, efficient, robust and inexpensive Cr:Colquiriite sources. However, Cr:Colquiriites have lower emission cross sections than Ti:Sapphire, ($1.3x10^{-20}$ cm^2 for Cr:LiCAF, 3% of Ti:Sapphire) that causes lower gain and higher tendency for Q-switching. Further, they have lower third-order nonlinearity ($0.4\ x10^{-16}$ cm^2/W for Cr:LiCAF, 12% of Ti:Sapphire) [34] which creates stability issues while

obtaining ultrashort pulses via makes Kerrlens mode-locking (KLM). Saturable Bragg reflectors (SBRs) [15] (also referred as saturable absorber mirrors (SESAMs) [14]), can overcome this limitation by enabling self-starting, robust and stable mode-locked operation. Cr:LiCAF was the first Cr^{3+}-doped colquiriite material in which lasing was demonstrated[31]. However, initially, it did not draw much attention, mostly due to the high level of parasitic losses (~2% per cm) observed in Cr:LiCAF during the early years of its production [35-38]. This high level passive losses in Cr:LiCAF rooted mostly from micrometer- sized or smaller precipitates arising during the growth process [35, 36], which obstructed efficient laser operation in this low-gain medium. On the other hand, compared to Cr:LiSAF, Cr:LiCAF has several advantages. Cr:LiCAF has superior thermal characteristics. It has the highest thermal conductivity and thermal lensing [39, 40]. Morever, Cr:LiCAF has lower quantum defect and the excited-state absorption[31]. These properties makes Cr:LiCAF the most appropriate Cr:Colquirrite crystal for the high power laser applications.

2.1 Semiconductor Saturable-Absorber Mirrors (SESAMs)

SESAMs are passive switches that are used to achieve mode-locking. A saturable absorber is a medium whose absorption coefficient decreases as the intensity of the light passing through it increases; it thus transmits intense pulses with relatively little absorption while absorbing weak ones. Therefore, when the phases of the different modes are related in such a way to form an intense pulse that can then pass through the switch, the oscillation condition is satisfied. SESAMs consist of an antiresonant semiconductor Fabry–Perot etalon formed by a semiconductor layer grown on top of a highly reflecting semiconductor Bragg mirror and covered by a dielectric reflector. The semiconductor layer typically consists of absorptive quantum-well layers in an otherwise transparent medium. The bandgap of the quantum wells can be engineered to provide saturable absorption at a wide variety of wavelengths.

The first intracavity SESAM device was the antiresonant Fabry–Perot saturable absorber (A-FPSA) [41]. Here, the Fabry–Perot is typically formed by the lower

semiconductor Bragg mirror and a dielectric top mirror, with a saturable absorber. The thickness of the total absorber and spacer layers are adjusted such that the Fabry–Perot is operated at antiresonance. Operation at antiresonance results in a device that is broad-band and has minimal group velocity dispersion. The top reflector of the A-FPSA is an adjustable parameter that determines the intensity entering the semiconductor saturable absorber and, therefore, the effective saturation intensity or absorber cross section of the device. The dielectric top reflector on the SESAM is generally designed to be highly reflecting at the wavelength of the pump light so that there is no pump-induced bleaching of the saturable absorber. The high-finesse antiresonant Fabry–Perot saturable absorber (A-FPSA) device Fig.2.1 shows a typical high-finesse A-FPSA design. The bottom mirror is a Bragg mirror formed by 16 pairs of AlAs–GaAs quarter-wave layers with a complex reflectivity. The multiple-quantum-well (MQW) absorber layer has a thickness chosen such that the antiresonance condition is fulfilled.

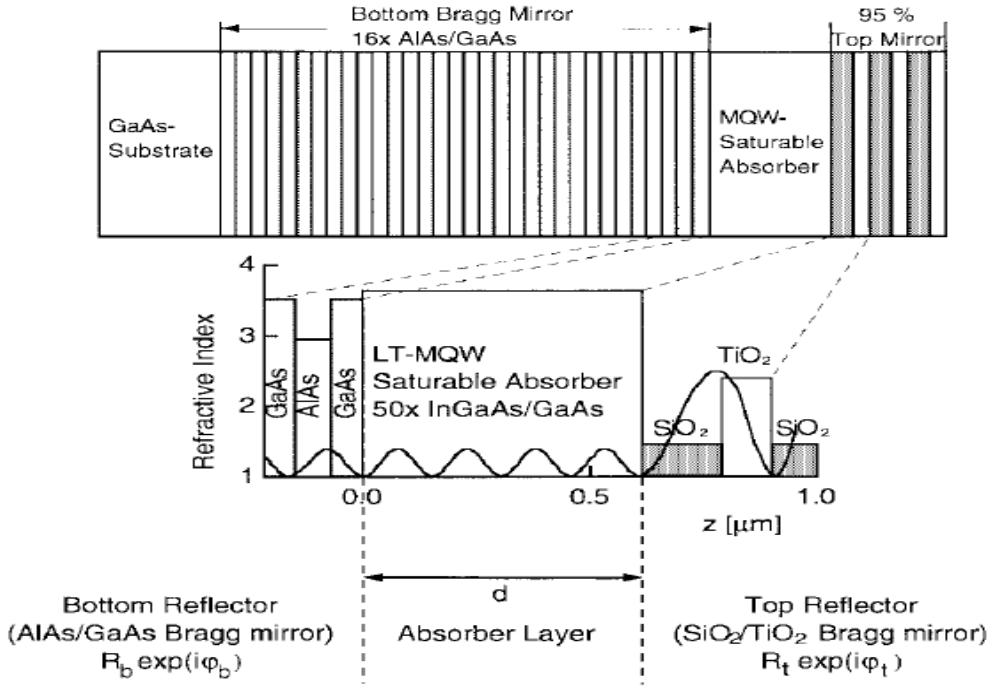

Figure 2. 1 *High-finesse A-FPSA: A specific design for a ~1.05 µm center wavelength laser. The enlarged section also shows the calculated standing-wave intensity pattern of an incident electromagnetic wave centered at 1.05 µm. The Fabry–Perot is formed by the lower AlAs–GaAs Bragg reflector, the absorber layer of thickness* $\bar{n}d = 4(\lambda/2)$ *and a top* SiO_2/TiO_2 *Bragg reflector, where* $\bar{n}$ *is the average refractive index of the absorber layer .(taken from[14]).*

Stable mode-locking with intracavity saturable absorbers has been achieved by varying the parameters such as response time and absorption cross section through special growth and design techniques. With SESAM's, we can benefit from control of both material and device parameters to determine the performance of the saturable absorber. We can view these as basic optoelectronic devices for ultrafast laser systems. One of the main limitations of SESAMs is their relatively low damage threshold. Typical values for the damage fluence of the semiconductor materials are $\sim 10 \mathrm{mJ/cm^{-2}}$. The damage fluence of the SESAMs can be increased beyond this value by using highly reflective dielectric layers. This, however, reduces the saturable loss, which generally reduces the *Q*-switched pulse energy and increases the pulse duration.

In our experiments, the epitaxial growth of the SBRs were performed at the Integrated Photonic Devices and Materials Group of MIT, in a solid source, multi-wafer, dual reactor molecular beam epitaxy (MBE) system (Veeco GEN 200), at typical AlGaAs growth temperatures. The 800-nm SBR consisted of twenty five pairs of $Al_{0.95}Ga_{0.05}As$ /$Al_{0.17}Ga_{0.83}As$ quarter wave layers for the Bragg mirror stack. The Bragg mirror stack is followed by five pairs of 6 nm thick GaAs quantum wells to provide the saturable absorber action.

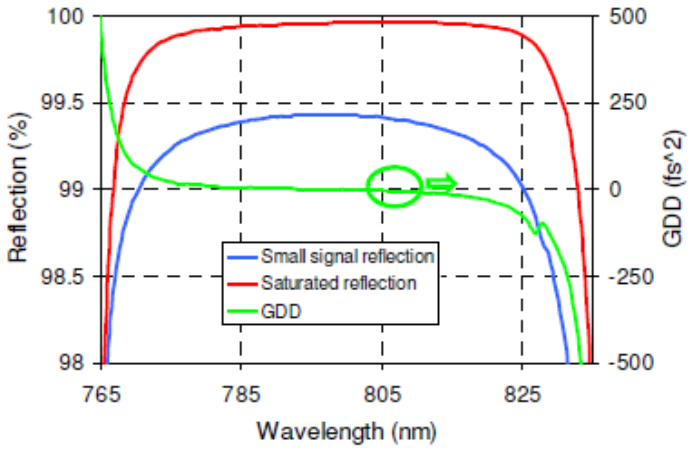

Figure 2. 2 *Calculated small signal reflection, saturated reflection and group delay dispersion (GDD) curves for the 800 nm SBR. The calculated modulation depth was(0.6 ± 0.2) % for the 800 nm SBR(taken from[42]).*

The quantum wells were sandwiched between 8 nm thick $Al_{0.17}Ga_{0.83}As$ barrier layers.$Al_{0.17}Ga_{0.83}As$ barrier layer had a thickness of 27 nm, which is then covered by a 5 nm thick GaAs cap layer. The thickness and the relative positions of the barrier layers and quantum wells were optimized to obtain almost wavelength independent linear and nonlinear absorption response from the absorber. Two additional pairs of $SiO_2 - TiO_2$ layers were also used as a high reflection coating to reduce the modulation depth of the 800-nm SBR to (0.6 ± 0.2) %. The 800-nm SBR had a saturation energy fluence of $\sim 35 \mu J/cm^2$

2.2 Tapered Diode Lasers (TDLs)

Laser diode arrays [39], broad-stripe single-emitter diodes [43-46], and single transverse-mode laser diodes (ridge waveguide lasers) [47-52] have been used to pump Cr:Colquiriite lasers to date. But, their relatively low brightness, requiring four to six diodes to reach reasonable output power levels was one of the main drawbacks of these sources [44, 53, 54]. For example, single mode diodes at 650 nm provide about 170 mW of output power at M^2 < 1.1. This corresponds to a brightness (B) of about 360 mW/μm2. Four of these diodes are needed to reach a cw output around 335 mW and average powers of about 250 mW in mode-locked operation [34].

Single-emitter diodes with 150 μm stripe width are commercially available and provide up to 1.5 W, but beam profiles are asymmetric and of low quality (M^2 slow~10, M^2 fast<1.1). Hence, even though they provide quite high output powers, their brightness (~340 mW/μm^2) is even lower than the single mode diodes. Therefore, one needs to combine two to four of these diodes to reach cw output levels of 590 mW and cw mode-locked average powers of 390 mW [46].

Likewise, multimode diode arrays might exhibit very high power levels (10s of Watts), but at the expense of increased cost and reduced beam quality [39]. For example, Kopf et al. used a 15 W diode array (M^2 slow~1200, M^2 fast<1.1, B ~28 mW/μm^2) to pump a specially designed Cr:LiSAF laser with an asymmetric cavity beam profile. Average powers of 1.42 W

and 500 mW were obtained in cw and cw mode-locked operation, respectively[39]. The low quality beam profile limited the cw slope efficiencies to 18% [39].

In summary, all studies performed so far have used complex pumping geometries to reach reasonable output levels from Cr:Colquiriite lasers due to the low brightness of the pump sources. Moreover, multimode diode pump sources with low beam quality induce strong thermal effects and only provide limited slope efficiencies in Cr:Colquiriite lasers [46, 52]. Multimode diode pumped Cr:Colquiriite lasers sometimes also require special optics for improving mode-matching between the pump and cavity mode (like cylindrical cavity mirrors [52] and coated flat-Brewster cut crystals [44], etc..), which increases cost and complexity of the overall system.

As an alternative technology, tapered diodes combine the excellent beam quality of ridgewaveguide lasers and the output power of broad-stripe single emitters [55, 56]. Tapered diode lasers consist of a straight ridge waveguide section and a tapered section as seen in Fig.2.3 Any higher-order modes generated in the tapered section are filtered out by the ridge waveguide, resulting in an almost diffraction-limited beam profile [55].

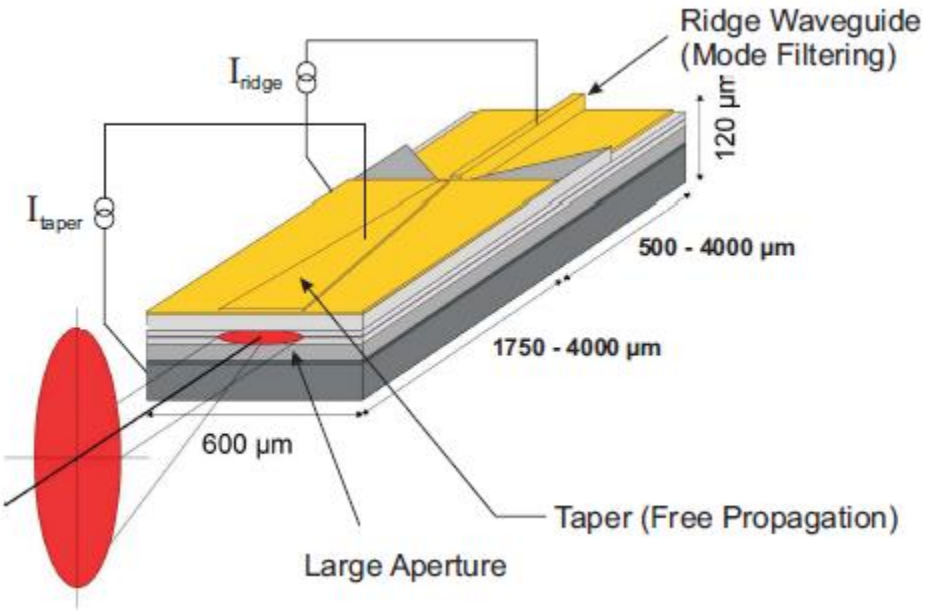

Figure 2. 3 *Lateral structure of a tapered laser (taken from [78]).*

In this work, we used monolithic high brightness tapered diode lasers (TDLs) to pump Cr:LiCAF system. A single device on a C-mount package [56] was used in the first set of experiments. It provided up to 1-W of output power at 675 nm together with M^2 ($1/e^2$) values of 5 in the fast axis and 1.5 in the slow axis, respectively. The TDLs used in tis study, were grown and characterized at the facilities of Ferdinand Braun Institute and detailed information on this class of diodes can be found in [56]. The TDL had a total cavity length of 2 mm, and consisted of a 500 μm long ridge waveguide section and a 1.5 mm long tapered amplifier section with a flared angle of 3°. The output aperture was 110 μm wide. The front facet of the TDL had a reflectivity of 1%, whereas the rear facet had a reflectivity of 94%. The device was mounted p-side down on copper tungsten submounts using AuSn solder, which was then mounted on standard C-mounts. A commercial temperature controlled c-mount diode fixture (ILX LDM-3095) was used in housing the diode.

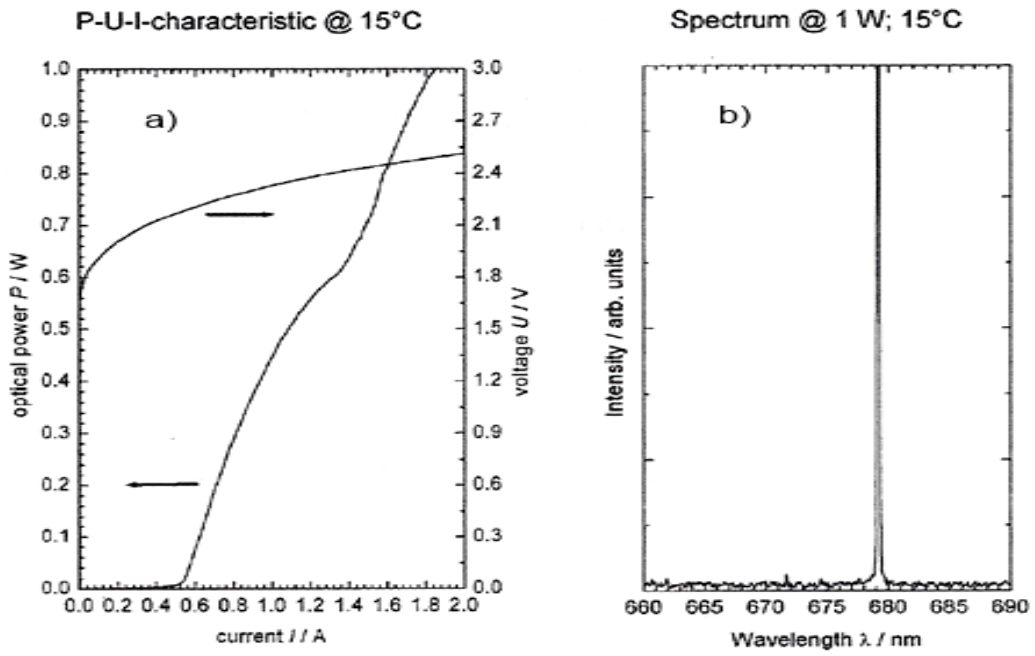

Figure 2. 4 *(Left) Measured variation of optical output power with input current for the tapered diode laser (TDL) at the diode holder temperatures of 15 °C. Corresponding voltage values of TDL. Measured optical spectrum of the diode at 1.6 A diode current, and at the diode holder temperature of 15 °C.*

Figure 2.4 (left) shows the measured variation of optical output power of the diode with drive current at a diode holder temperature of 15 °C. At this temperature, the diode had a lasing threshold of about 520 mA and a slope efficiency of about 1.06 W/A. The diode spectrum (Fig.2.4 right) had a width of 0.8 nm and was centered around 679.2 nm at 15 °C. At a drive current of 2 A, the diode provided up to 1.05 W of output power, with a diode voltage of 2.51 V, which corresponds to an electrical-to-optical conversion efficiency of about 21%. We note here that direct diode pumping with such an efficient diode provides a significant advantage to Cr:Colquiriites over Ti:Sapphire in terms of the overall electrical-to-optical conversion efficiency of the system. Our findings indicate that tapered diodes in the red spectral region are likely to become the standard pump source for Cr:Colquiriite lasers in the near future.

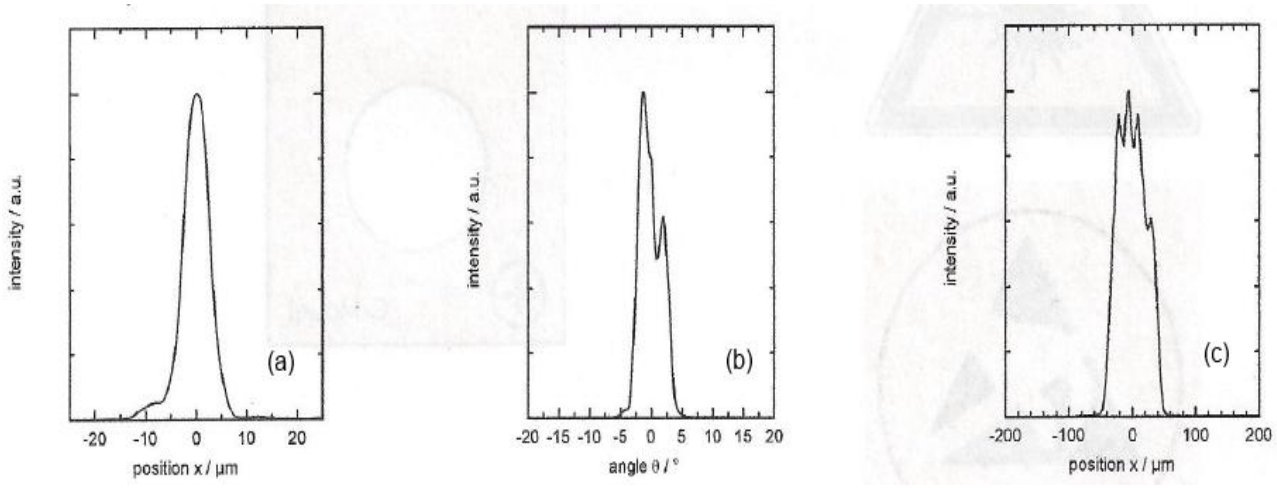

Figure 2. 5 *(a) Beam waist, (b) far field and (c) near field profile for the slow axis of the first tapered diode laser (TDL) measured at 1 W of output power and at a cooling temperature of 15 °C.*

Figure 2.5 shows the measured beam waist, far field and near field profiles of the first tapered diode laser in the slow axis. The measurements in Fig.2.5 were carried out at an output power of 1 W, and at the diode holder temperature of 15 °C. The measured beam waist is 10.1 µm at the $1/e^2$-level. 96% of the emitted power originates from the central lobe of the

beam waist. The corresponding far field angle is 6.7° ($1/e^2$), The astigmatism of the diode (the difference between the positions of the vertical and lateral beam waist) is measured to be 200 μm.

2.3 Continuous-Wave Lasing Experiments

A schematic of the continuous-wave Cr:LiCAF laser cavity is shown in Fig.2.6. The beam emitted by tapered diode was first collected by an aspheric lens of a focal length of 4.5 mm and was collimated in the slow axis. In the fast axis, the cylindrical lens of a focal length of 50 mm adjusted the collimation of the the diode output to obtain similar divergence in both axes. Then, it was focused into the crystal using a 60 mm focal length achromatic doublet. An astigmatically compensated, x-folded laser cavity was exercised in the cw laser experiments. The resonator had two curved mirrors (M3–M4, R = 50 mm), a GTI mirror, and a flat output coupler (OC). The high reflectivity of the cavity mirrors (M3–M4) extended from 750 nm to 850 nm and had reflectivity around 99.99%. The total cavity length was 122 cm. From the Standard ABCD analysis of the cavity, the beam waist inside the Cr:LiCAF was determined to be 25μm.

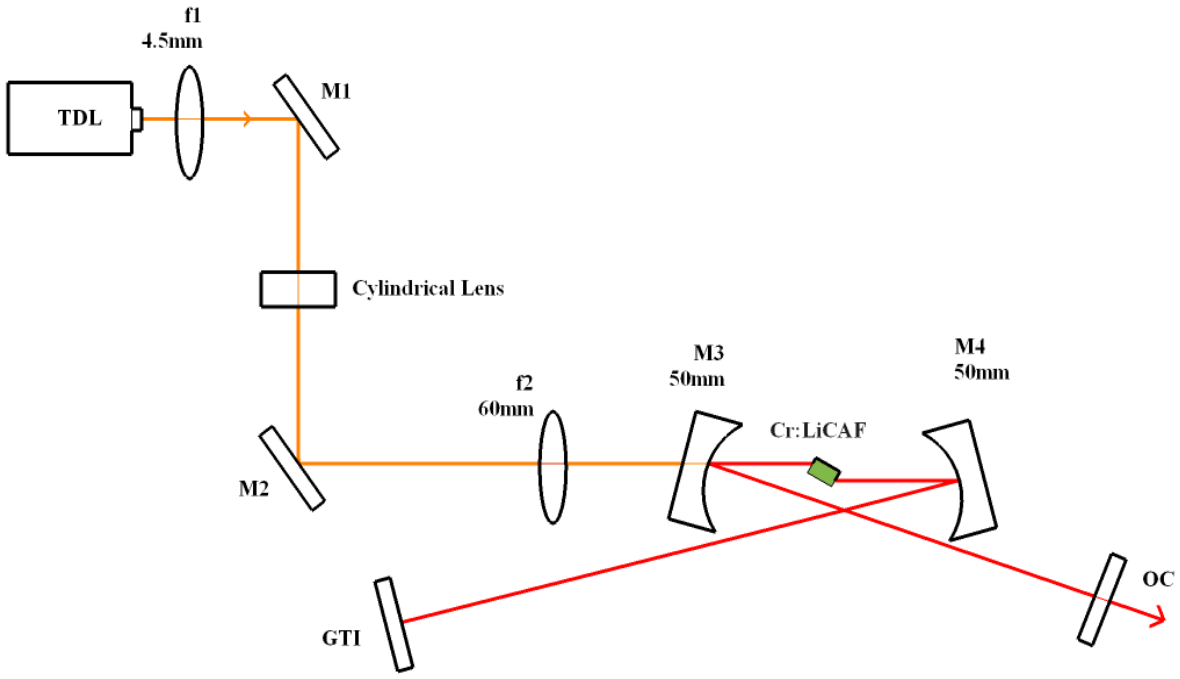

Figure 2. 6 *Schematic of the cw Cr:LiCAF laser setup. The x cavity is end-pumped by a 1-W taperd-diode laser (TDL) at 675 nm.*

The 7% Cr-doped Cr:LiCAF boule that was used in this study was grown from nearly stoichiometric melts of the components LiF, AlF_3, CrF_3, CaF_2, by the Czochralski method. To avoid scattering centers that are typical for Cr:LiCAF, slow pulling rates were applied(~0.5 mm⁄h) and flat temperature gradients were maintained during the growth. Usage of superior-quality starting materials and preparation under dry conditions were also necessary for the growth of high quality Cr:LiCAF crystals (passive losses below 0.15% per cm). More details on growth of high quality Cr:LiCAF crystals can be found in [37]. The 5 mm long, 1 mm thick, Brewster-cut laser crystal was used in the studies, which absorbed about 95% of the incident TM polarized pump light. The crystal was mounted with indium foil in a copper holder. The pump source is a 675 nm TDL, which provides up to 1 W of output power at an electrical-tooptical conversion efficiency of 20%.

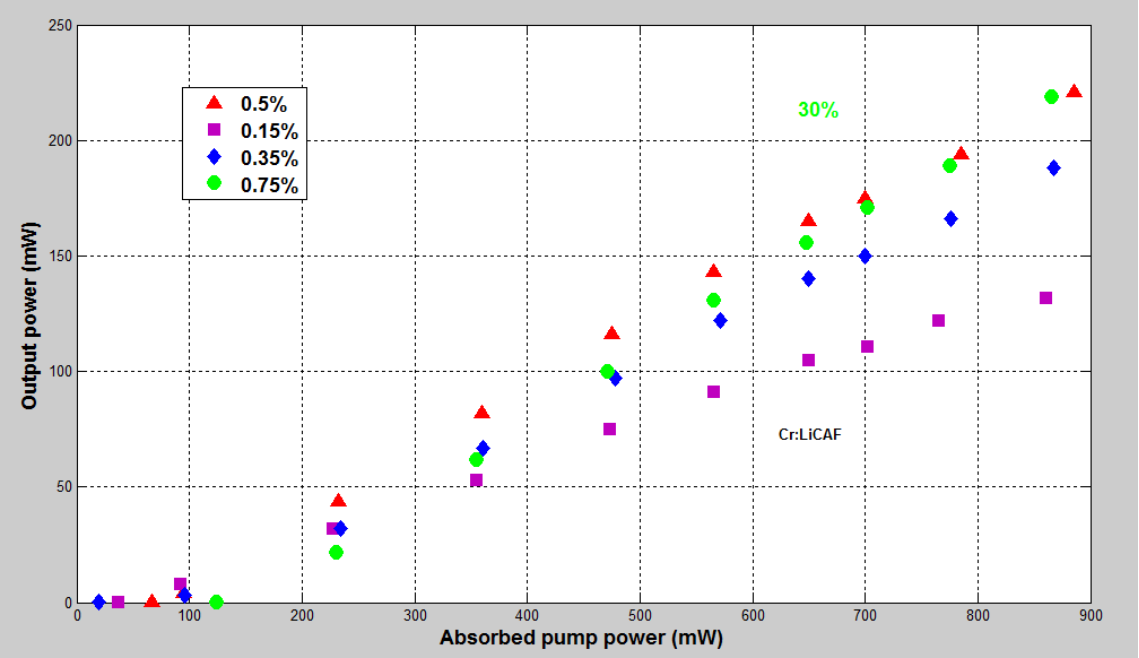

Figure 2. 7 *Continuous-wave output power versus absorbed pump power for the single tapered diode pumped Cr:LiCAF laser taken at various levels of output coupling between 0.5 and 3%.*

The cw laser efficiencies of Cr:LiCAF at various levels of output coupling are depicted in Fig. 2.7. All data were taken at a base temperature of the crystal mount of 20 °C. An output power of 220 mW was obtained with the Cr:LiCAF laser at an absorbed pump power of 885 mW and with a 0.5% of output coupling mirror. A lasing threshold of 95 mW and a slope efficiency of 30% have been determined for this system. Due to the increased role of parasitic losses, obtainable power levels decreased with 0.15% of output coupling.

2.4 Mode-Locking Experiments

In this section mode-locking configuration of the cavity with a semiconductor saturable absorber mirror is presented in detail. Experimental results are presented and discussed in mode-locked regime.

2.4.1 Experimental Setup

Figure 2.8, shows a schematic of the Cr:LiCAF laser that is exerted in mode-locked laser experiments. A SBR [15], also referred to as semiconductor saturable absorber mirror (SESAM) [14], was used to initiate and sustain mode-locked operation. The SBR had a central reflectivity around 800 nm and an estimated modulation depth of (0.6 ± 0.2)%. A 100 mm radius of curvature mirror (M5) was exploited to focus the intracavity beam tightly on the SBR to provide the necessary fluence for stable cw mode-locked operation. In mode-locked laser experiments, negative cavity dispersion is also provided to operate the laser in soliton mode-locked regime. In this regime, the net cavity dispersion should be adjusted to balance the self phase modulation from the crystal. The net amount of cavity dispersion together with the self phase modulation determines the output pulsewidth. Hence, one can tune the amount of cavity dispersion to adjust the pulsewidth to the desired value. In this study, our primary aim was not to obtain short pulses, thus we did not study on the amount of dispersion. For obtaining femtosecond level pulses, GTI mirror M5 with group velocity dispersion of about -550 fs^2per bounce were inserted to provide the required negative dispersion. The estimated total round-trip cavity dispersion was about -960 fs^2 ($+125$ fs^2 from 5 mm of 7%-doped Cr:LiCAF, $+15$ fs^2 from 122 cm of intracavity air).

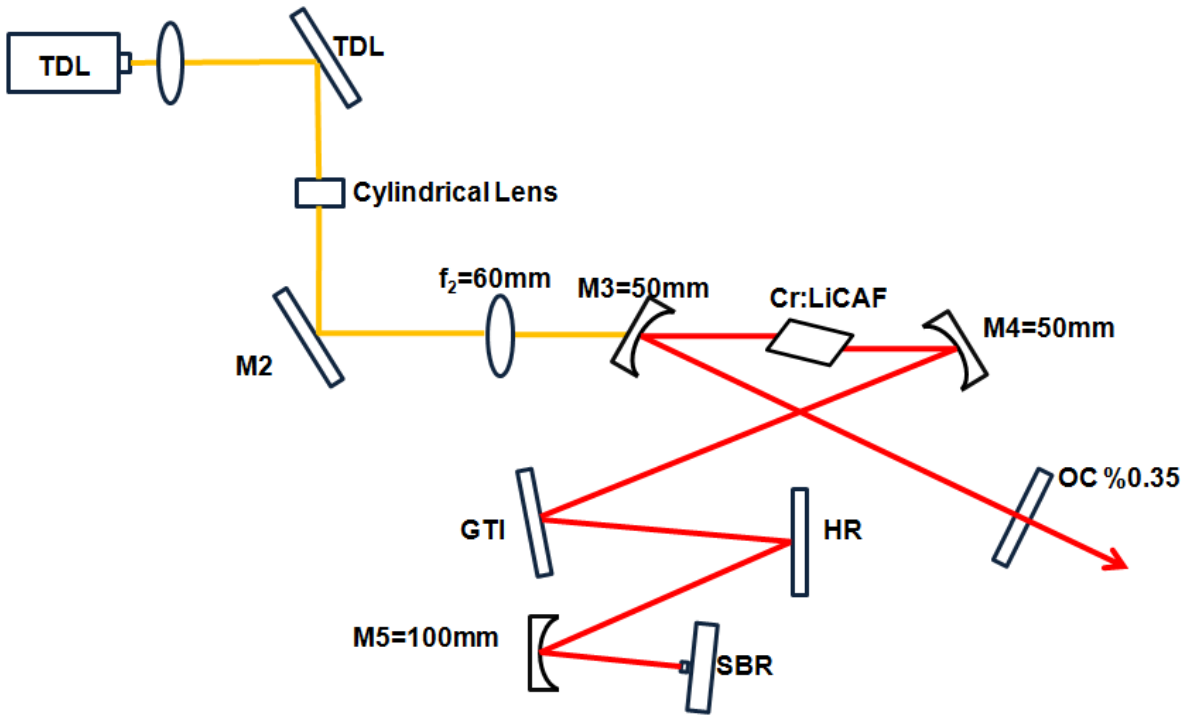

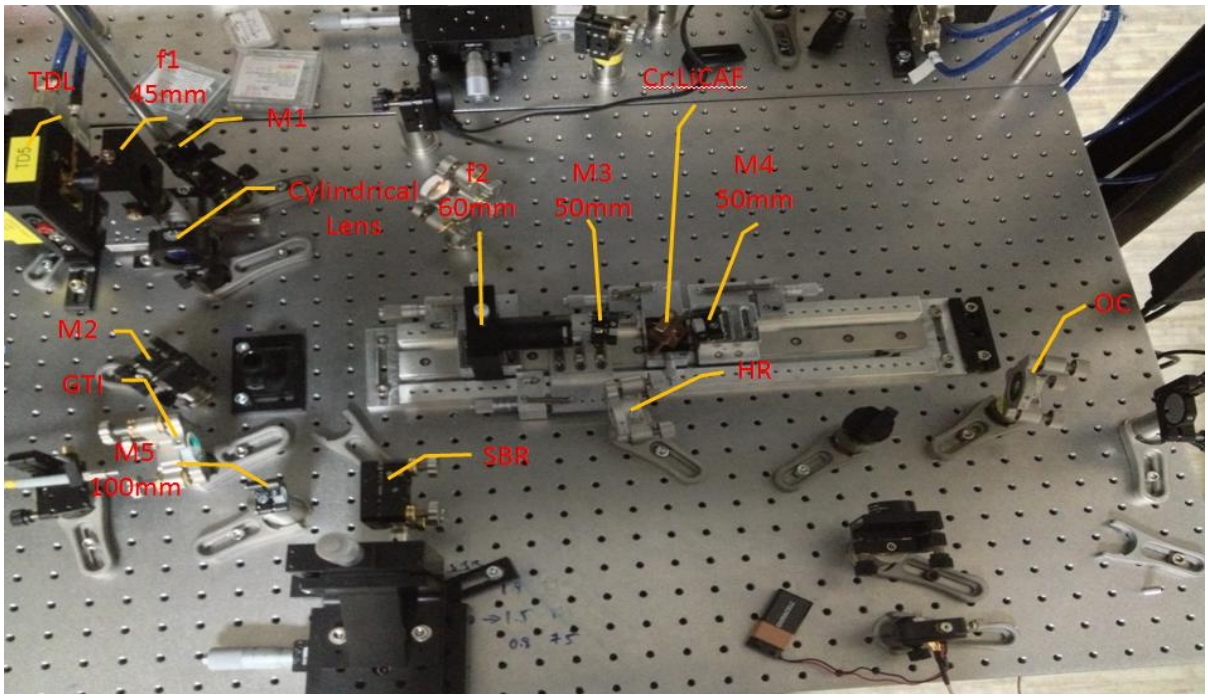

Figure 2. 8 *Schematics of cw mode-locked Cr:LiCAF oscillator pumped by a single tapered diode laser (TDL-1). SBR: Saturable Bragg reflector. M3-M4: Curved pump mirrors with a ROC of 50 mm. OC: Output coupler,. f1: Collecting and collimating aspheric lens. f2: Focusing lens.*

To obtain stable cw mode-locking, the spot size on the SBRs was optimized by varying the radius of curvature of the focusing mirror and by fine adjustment of the SBR position with respect to the focusing mirror. In general, a too large spot size on the SBR causes problems in initiating mode-locking or might cause Q-switched mode-locked laser operation. On the other hand, a too tight focus on the SBR, might cause double pulsing (or pulse break up) and SBR damage. The necessary focusing level is also dependent on the pulsewitdh and on the intracavity energy level. However, once the spot size on the SBR was adjusted to the correct range, the SBR mode-locked laser is self-starting and operates as a turn-key system requiring little adjustment due to mechanical thermal misalignments.

2.4.2 Mode-Locking Results

In this section, cw mode-locking data with the one TDL diode pumped Cr:LiCAF laser will be presented. As mentioned earlier, the laser is mode-locked with an SBR. For SBR mode-locked lasers, to obtain stable cw mode-locking, one needs to be above a critical intracavity pulse energy $E_{P,c}$. Under several simplifying assumptions, one can express $E_{P,c}$ as [17, 57]

$$E_{P,c} = \sqrt{\frac{h\nu_l}{(m\sigma_{em})} A_{eff,L} F_{sat,A} A_{eff,A} \Delta R}, \tag{2.1}$$

where:

m is the number of passes through the laser crystal in one round trip, $A_{eff,L}$ ($A_{eff,A}$) is the effective laser mode area inside the gain medium (on the SBR), $F_{sat,A}$ is the absorption saturation fluence of the SBR, ΔR is the modulation depth of the SBR.

Cr:LiCAF gain medium has a quite low emission cross section ($1.3 \times 10^{-20}\, m^2$), which is more than 30 times smaller than of Ti:Sapphire ($41 \times 10^{-20}\, m^2$) [34]. Hence,

Cr:LiCAF systems have high tendency for Q-switched mode-locking. This makes obtaining pure cw mode locking challenging in Cr:LiCAF laser systems. However, our experiments have shown that it is still possible to obtain stable cw mode-locked operation from low-pump-power Cr:LiCAF lasers at repetition rates over 100 MHz. Figure2.9, shows a representative mode-locking data we have taken from the Cr:LiCAF laser using a 0.35% transmitting OC, at the repetition rate of 120 MHz. At the full pump power of 915 mW, the laser produced 340 fs long pulses with 51 mW of average mode-locked output power. The corresponding pulse energy and pulse peak power was 425 pJ and 1.1 kW, respectively. The time-bandwidth product of the pulses was 0.364, which is close to the transform limit of 0.315 for sech^2 pulses.

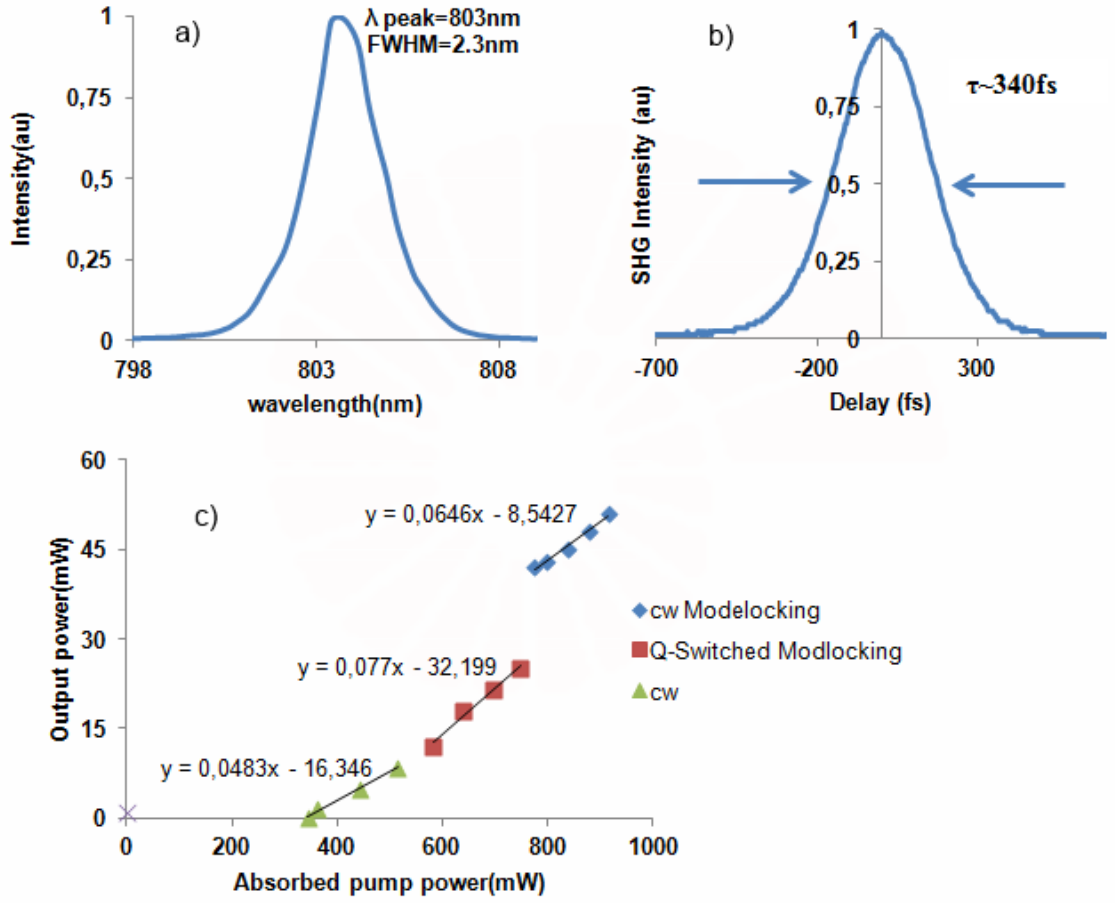

Figure 2. 9 *(a) Optical spectrum, (b) autocorrelation data, and (c) Output power versus absorbed pump power versus absorbed pump power*

Figure 2.9 summarizes representative mode-locking data of Cr:LiSAF laser around 800 nm. The estimated net cavity dispersion was about -985 fs^2. Fig. 2.9(c) shows the variation of laser output power and laser dynamics with absorbed pump power, using the 0.35% output coupler. The laser operated in cw mode for absorbed pump powers up to 580 mW, and generated Q-switched mode-locked pulses for pump powers between 640 mW and 780 mW. Stable cw mode-locking was obtained for pump powers above 780 mW. The crystal holder was cooled to 20 °C and the maximum output power was ultimately limited by thermal effects. The spectrum was centered near 803 nm and had a spectral bandwidth of 2.3 nm.

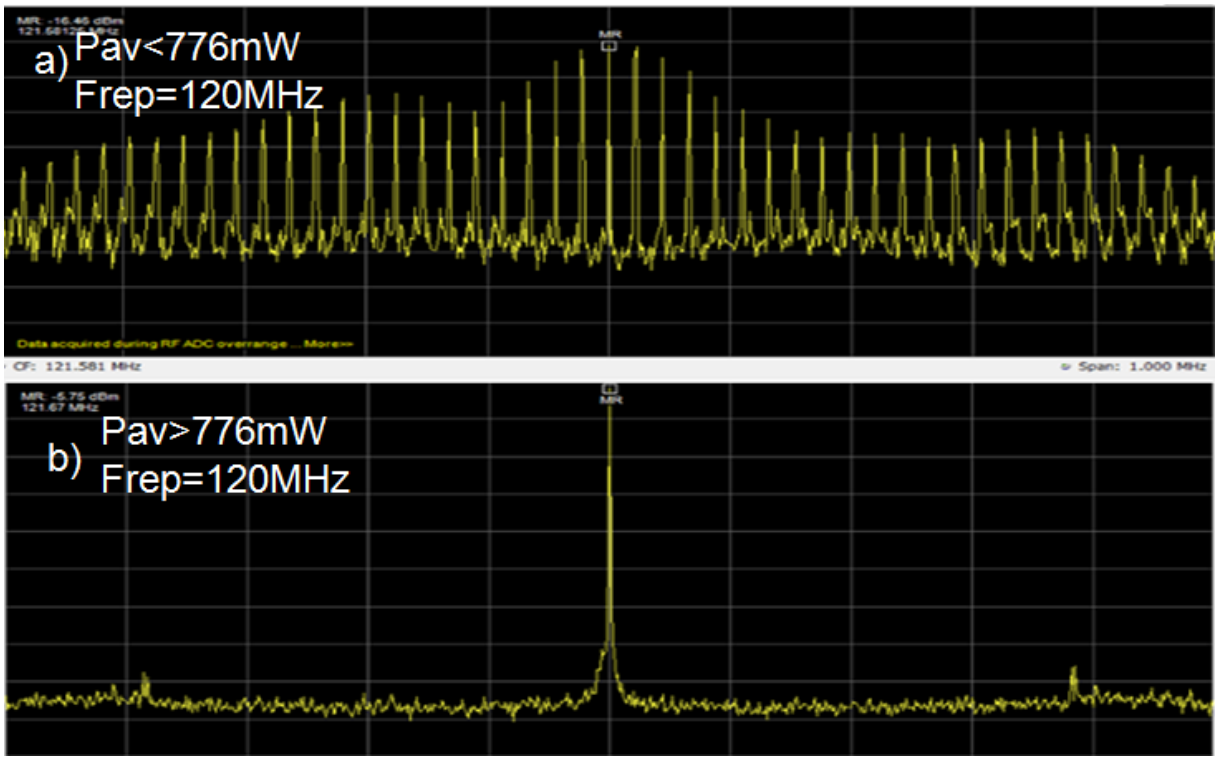

Figure 2. 10 *a) RF spectrum of Q Switched pulses below 776mW input power. b) RF spectrum of cw Mode Locked 340 fs pulses centered around 800 nm from the Cr:LiCAF laser. This cavity had an OC of 0.35% and a repetition rate of 120 MHz.*

Further, the pulses also had a clean RF spectrum where the main peak at 121 MHz was around 120 dB above the noise floor as shown in Fig.2.10. Lastly, we have also tried

obtaining higher repetition rates at 200 MHz. However, we could only obtain Q-switched pulses using 0.1% OC with an average output power of 15mW.

2.5 Summary and Future Work

In this study, we have investigated a minimal-cost and minimal-complexity Cr:LiCAF laser that is pumped by a high brightness tapered diode laser. Cw and cw mode-locked operation conditions have been investigated. When mode-locked, using an SBR, the Cr:LiCAF laser produced 340 fs longpulses around 800 nm at average powers of 50 mW.

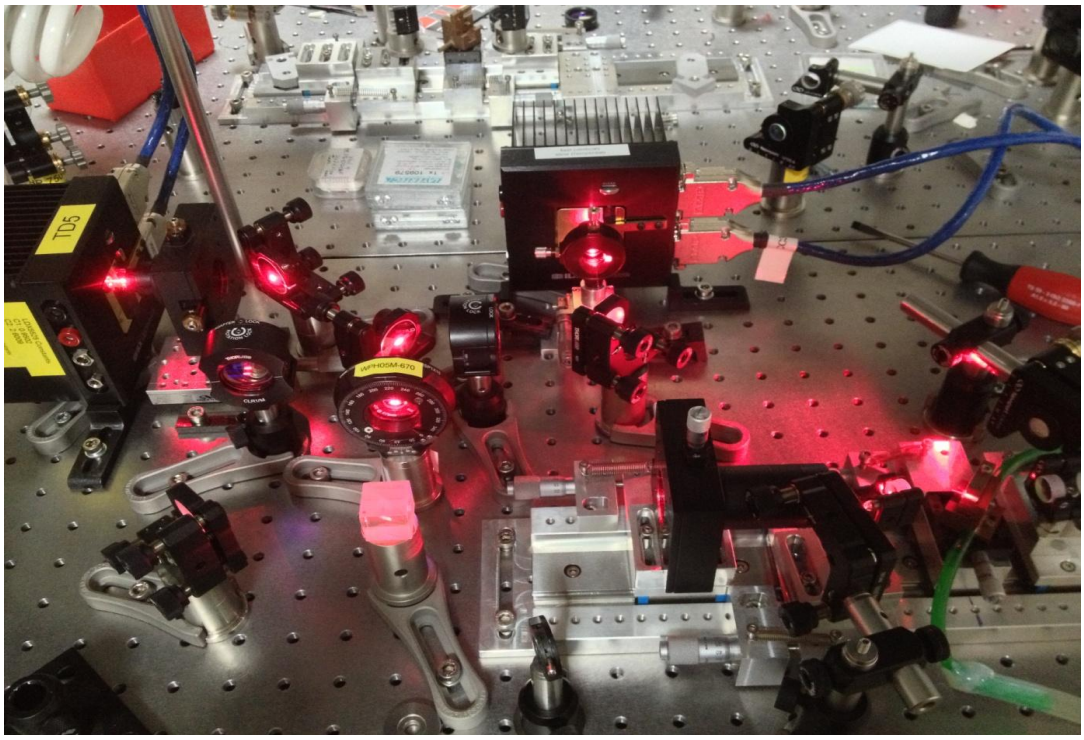

Figure 2. 11 *Cr:LiCAF laser that is pumped by two tapered diodes. Diodes lights are combined via polarization coupling using a beam splitter cube.*

Our results show that a single TDL is not sufficient to obtain high repetition rates from Cr:LiCAF lasers. We have added the second TDL into our system (Fig.2.11) to reach higher frequencies, however above 200MHz repetition rates, tight focusing and the energy of the pulse on the SBR caused the damage of the SBR, but there is great potential to reduce te

thermal damage in future studies. The availability of tapered diode pump sources with higher electrical to optical conversion efficiencies is expected to increase the output power of the laser and make it possible to obtain high repetition rates up to or beyond 1 GHz. Our future research efforts will focus on obtaining GHz level pulses with sub-100-fs duartion at average powersaround100mW.

Chapter 3: Generation of Terahertz Radiation by a Multipass-Cavity Mode-Locked Ti:Sapphire Femtosecond Laser

3.1 THz Pulse Generation and Detection Methods

Terahertz (THz) region of the electromagnetic spectrum lies between the optical frequencies and the microwave frequencies as can be seen in Fig.3.1. The definition of THz gap generally covers the region from 300GHz(λ=1mm) up to 10 THz (λ=30μm). Researchers did not extensively explore the THz gap because they lacked reliable sources of terahertz radiation. However, the demands come from two dramatically different groups: 1) ultrafast time-domain spectroscopists who wanted to work with longer wavelengths, and 2) longwavelength radio astronomers who wanted to work with shorter wavelengths. Both of these demands have led to the development of Terahertz science. Early in the 1990s, the field of terahertz (THz) optoelectronics, dramatically improved because of the development of semiconductor technology and the availability of short optical pulses, especially those of femtosecond laser pulses (Ti:sapphire femtosecond lasers became commercially available). After then, "THz-pulse" began to be used to express ultrafast EM transients. With the advances in the photoconductive antenna and electro-optic sampling techniques, the field became open to spectroscopy and imaging related studies. Much of the recent interest in terahertz radiation stems from its ability to penetrate deep into many organic materials without the damage associated with ionization. Because the terahertz radiation is readily absorbed by water, it can be used to distinguish between materials with varying water content. These properties lend themselves to applications especially in biomedical imaging. In this study, we aimed at generating THz radiation by using a photoconductive antenna and optical rectification

techniques with a low cost, high power Ti:sapphire multipass cavity (MPC-Ti:A_2O_3) femtosecond laser operating around 800 nm.

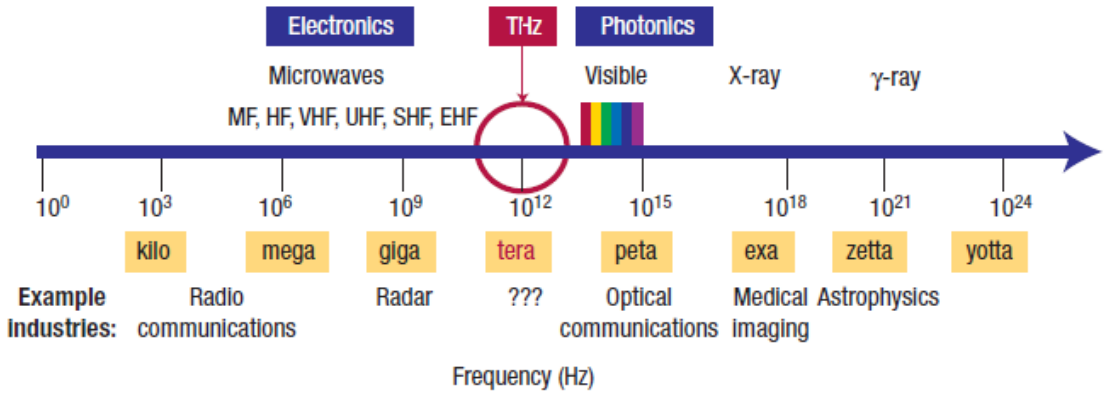

Figure 3. 1 *The electromagnetic spectrum. (taken from Ref.[58])*

In the following paragraph, a brief historical review of milestones of the field are presented following Ref.[43].

In 1984, *Auston*, *Cheung* and *Smith* [59] reported an experiment that is now regarded as the origin of the current booming optoelectronic THz Technologies. They were able to generate approximately 1.6 ps electromagnetic (EM) pulses, let them propagate freely and detect them coherently using such a configuration as the PC switch arranged symmetrically on opposite sides of a dielectric slab. The radiation source was the ultrafast transient current in the PC switch and the detection was performed coherently by sampling the repetitively incident EM pulses. They used 100 fs optical pulses from a colliding-pulse passively mode-locked (CPM) ring dye laser and radiation-damaged Si-on-sapphire (RD-SOS) for the experiment.

In 1988, *Smith*, *Auston* and *Nuss* [60] showed a refined antenna structure with the PC dipole on RD-SOS. They used the antenna both as an emitter and a detector, and tested by pumping the center of each dipole with 120 fs optical pulses from a CPM dye laser for coherent emission and detection. It was revealed that such dipoles have frequency spectra that extend from ≈ 100GHz to over 1THz and this paper is regarded as the first paper that

mentioned that the EM transient emitted from the PC antenna involves THz frequency components.

In 1989, van Exter, Fattinger and Grischkowsky [61] showed a refined dipole antenna with a coplanar transmission line, introduced by Ketchen et al. [62], to match the pulse generated in the gap with the propagating modes, and showed an EM beam system including GHz and THz frequency components with off-axis paraboloidal mirrors and with a lens on each PC dipole. Furthermore, they characterized their EM beam system precisely and showed that the system is useful as a spectroscopic tool (terahertz time-domain spectroscopy, THz-TDS) [63].

Early in the 1990s, Ti:sapphire femtosecond lasers became commercially available and THz optoelectronics began to spread all over the World and the word "THz-pulse" began to be used to express ultrafast EM transients. At almost the same time as the Ti:sapphire sub-100 fs laser was brought to market, the molecular-beam-epitaxy (MBE) grown low temperature GaAs (LT-GaAs) thin films began to be used. The carrier lifetime of LT-GaAs is controlled by the substrate temperature in epitaxial growth by MBE. It has the shortest carrier lifetime compared to any other materials, while keeping relatively high mobility. Since then, infinitesimal dipoles, or Hertzian dipoles, fabricated on LT-GaAs substrate have been used frequently as an emitter or detector driven by PC shortening the dipole gap pumping with a sub-100 fs Ti:sapphire laser. On the other hand, until recently it was believed that the bandwidth of the PC antenna is limited to below about 7 THz, but very recently *Kono* et al. [64-66] have broken the limitation and extended the upper limit to as high as 60 THz with the use of 15 fs light pulses.

3.1.1 Terahertz-Pulse Emission from Photoconductive Antennas

THz pulses have been generated by different methods, such as irradiation of PC antennas, semiconductor surfaces, or quantum structures with femtosecond optical pulses. Among these methods, THz-pulse emission from the PC antenna is crucial and fundamental. In Terahertz Time Domain Spectroscopy, THz pulses are genarally generated either by potoconductive antennas or optical rectification techniques.

THz generation with photoconductive antennas is based on the rapid change in conductivity of a fast response material with the optical excitation by ultrafast laser pulses. The charge carriers created in the depletion region of a semiconductor surface triggered by an ultra fast laser pulse provides electromagnetic radiation in the THz spectral region.

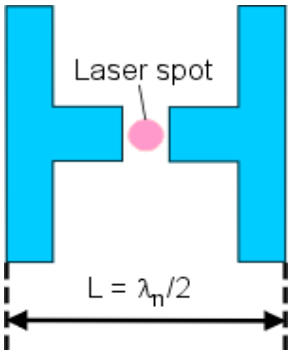

Figure 3. 2 *The analogy of the photoconductive antenna with a Dipole antenna of a length L(taken from Ref.[78])*

The photoconductive antenna can be considered as a dipole of length L, which is in resonance with the electromagnetic wavelength λ_n inside the semiconductor. The resonance condition is $L = m * \lambda_n/2$ with $m = 1,2,3, \dots integer$. The wavelength λ_n in the material with the refractive index n is given by $\lambda_n = \lambda/n$. Using the wave relation $c = \lambda * f$ and $m = 1$, the resonance frequency f of the antenna is given by

$$f = c/(2 * n * L) \tag{3.1}$$

where:

$c = 3\times10^8$ m/s - speed of light in the vacuum,
n = refractive index of the semiconductor antenna material,
L = length of the antenna.

Figure 3.3 shows a standard THz pulse generation scheme. For the construction of the PC antenna, a PC substrate with short carrier lifetime, high mobility and high breakdown voltage is needed. Historically, such PC materials shown in Table 1 were used.

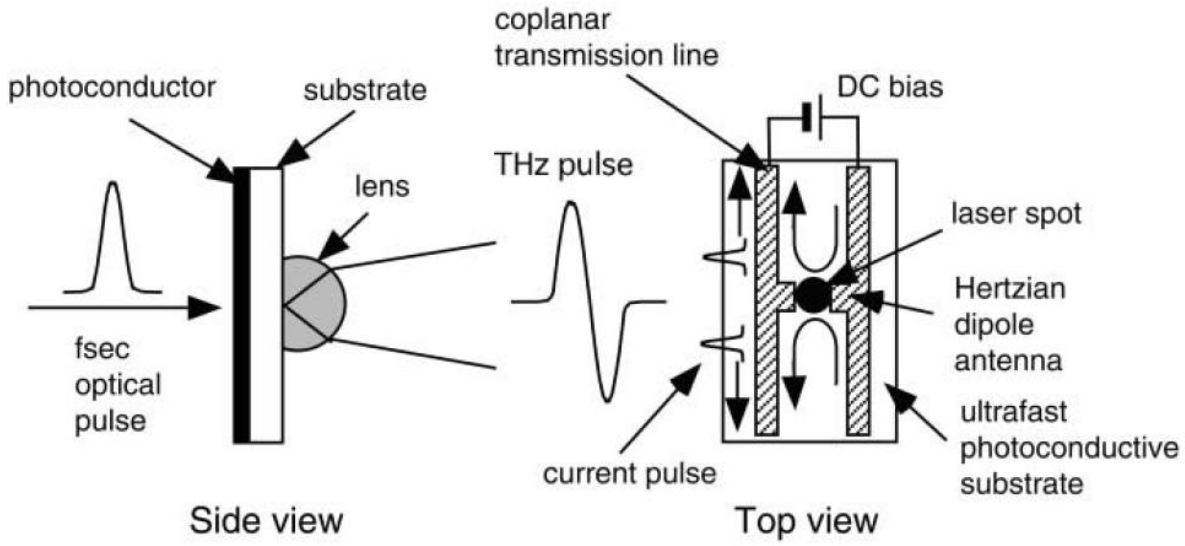

Figure 3. 3 *Standard THz-pulse generation from a PC antenna pumped with a femtosecond optical pulse. Propagation of current pulses along the coplanar transmission line are shown in the top view(taken from Ref. [67])*

Photoconductive materials	Carrier lifetime (ps)	Mobility ($cm^2/(V \cdot s)$)	Resistivity ($\Omega \cdot cm$) (Breakdown field, V/cm)	Band gap (eV at R.T.)
Cr:doped SI-GaAs	50–100.0	$\approx 1\,000$	10^7	1.43
LT-GaAs	0.3	150– 200	10^6 (5×10^5)	1.43
SI-InP	50–100.0	$\approx 1\,000$	4×10^7	1.34
Ion-Implanted InP	2– 4.0	200	$> 10^6$	1.34
RD-SOS	0.6	30		1.10
Amorphous Si	0.8– 20.0	1	10^7	1.10
MOCVD CdTe	0.5	180		1.49
LT-$In_{0.52}Al_{0.48}As$	0.4	5		1.45
Ion-implanted Ge	0.6	100		0.66

Table 3. 1 *Characteristics of ultrafast photoconductive materials(taken from Ref [67])*

Due to their improved subpicosecond carrier lifetime, relatively high carrier mobility, and high breakdown fields LT-GaAs layers have been extensively studied for ultrafast optoelectronic applications. The properties of the LT-GaAs depend on both the growth conditions during the MBE process and on the postgrowth annealing. We now describe the physical properties of a THz emitter system based on the PC antenna shown in Fig. 3.3 right, which behaves as a Hertzian dipole. When the PC gap is pumped with femtosecond optical pulses with an energy greater than the bandgap of the semiconductor (Eg = 1.43 eV for GaAs at room temperature), free electrons (holes) are generated in the conduction (valence) band. The carriers are then accelerated in phase by the bias field and decay with a time constant determined by the carrier lifetime, resulting in a pulsed photocurrent (or a step-function-like photocurrent in long-carrierlifetime semiconductors) in the PC antenna. Current modulation occurs in the subpicosecond regime and thus emits a subpicosecond electromagnetic transient, i.e. a THz pulse. For an elementary Hertzian dipole antenna in free space, the far field radiated electric field $E(r, t)$ at a distance r (much greater than the wavelength of the radiation) and time t is described as

$$E(r,t) = \frac{l_e}{4\pi\varepsilon_0 c^2 r}\frac{\partial J(t)}{\partial t}\sin(\theta) \propto \frac{\partial J(t)}{\partial t} \tag{3.2}$$

where:

$J(t)$ *is the current in the dipole,*

l_e *is the effective length of the dipole,*

ε_0 *is the dielectric permittivity of vacuum,*

c *is the velocity of light in vacuum,*

θ *is the angle from the direction of the dipole.*

Equation (3.2) indicates that the radiation amplitude is proportional to the time derivative of the transient photocurrent $\frac{\partial J(t)}{\partial t}$ and the effective antenna length l_e.The photocurrent density is described as [68]

$$j(t) \propto I(t) \otimes [n(t) q v(t)] \tag{3.3}$$

where:

$\otimes$ *denotes the convolution product,*

$I(t)$ *is the optical intensity profile,*

q *is the charge,*

$n(t)$ *is the density,*

$v(t)$ *is velocity of the photocarriers.*

The dynamics of the photogenerated free carriers in a semiconductor is well described by the classical Drude model. According to this model, the average velocity of the free carriers obeys the differential equation

$$\frac{dv(t)}{dt} = -\frac{v(t)}{\tau} + \frac{q}{m} E(t) \tag{3.3}$$

where:

τ *is the momentum relaxation time,*

m *is the effective mass of the carrier.*

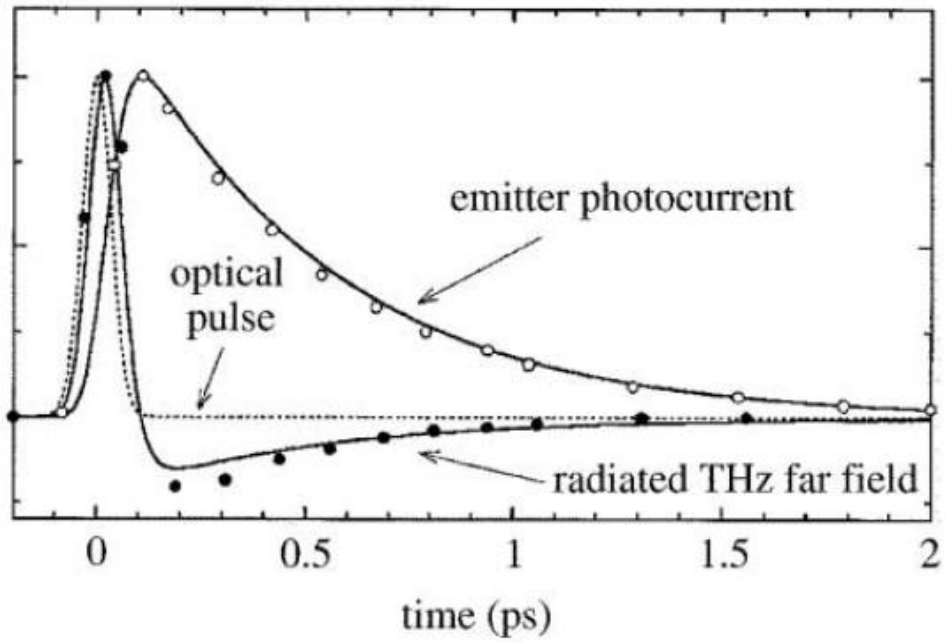

Figure 3. 4 *Calculated photocurrent in the emitter and amplitude of the radiated field as a function of time. The temporal shape of the optical pulse is drawn as a dotted line. Ref.[68]*

The current density $n(t)qv(t)$ represents the impulse response of the PC antenna, i.e. the response to a delta-function-like optical pumping. Figure 3.4 shows a typical temporal behavior of the photocurrent density in the emitter and of the associated radiated THz far field. Here, the temporal shape of the optical pulse is assumed to be Gaussian. As illustrated in Fig.3.3 left (side view), the generated THz pulse is emitted from the substrate side.

3.1.2 Optical Rectification

A pulsed wave with a central frequency in the optical band and spectral width in the THz range can be down-conwerted into a pulse of THz radiation via nonlinear crystal. When light interacts with a second-order nonlinear medium and wave mixing between two frequencies w_1 and w_2 occurs, two of the possible outcomes are sum-frequency generation and difference-

frequency generation, yielding radiation at the respective frequencies of $w_1 + w_2$ and $w_1 - w_2$. Thus, the high-frequency components can mix with the low-frequency components within a given pulse to produce a pulse at the difference frequency. Since the optical pulses have a bandwidth of a few THz, the difference frequencies fall in the THz range.

One advantage of optical rectification is that it is a nonresonant method and the THz pulse width is limited only by the optical laser pulse width (and the phonon-mode absorptions of the crystal), and not the response time of the material. Optical rectification is used for producing broadband THz radiation. Some of the shortest THz pulses to date, displaying bandwidths up to 100 THz, have been generated in this or a similar fashion [69-72].

3.1.3 Electro-optic Sampling

As mentioned earlier, the photoconductive antennas can be used for detection. When the ultrafast laser pulse creates charge carriers inside the semiconductor, the incoming THz pulse accellerates the charge carriers towards the electrodes of the antenna. The potential created is measured by the lock-in amplifier. Terahertz detection by photoconductive antennas will not be detailed here. Because it is nothing but the reverse process of the Terahertz generation from the photoconductive antenna. In this section, the electro optic sampling which is another widely used detection method in Therahertz Time Domain Spectroscopy will be briefly discussed.

The THz radiation is typically detected by Electro-optic Sampling (EOS) in a 0.5-1.0 mm thick <110> ZnTe crystal, although for high-bandwidth applications it must be as thin as $10\mu m$. It is based on the Pockels effect in which an applied voltage causes the detector crystal to become birefringent. When the optical sampling pulse travels through the crystal at the same time as one point in the THz pulse, its polarization is slightly rotated. The magnitude of the rotation is proportional to the magnitude of the THz field, and the direction of rotation is proportional to the sign of the field. In this manner, the entire pulse amplitude as a function of time is mapped out by scanning the delay line that determines when the readout pulse arrives at the detector crystal relative to the THz pulse [73]. The signal is collected with a lock-in

amplifier phase-locked to an optical chopper, which modulates either the THz generation arm or the pump beam (when a pump-probe experiment is performed). The THz beam path from the transmitter to the receiver is usually enclosed and purged with dry nitrogen to minimize THz absorption by water vapor. Ref. [74] provides a detailed analysis of the electro-optic sampling method.

3.2 Experimental Setup and Results

In this section, after explaining some details of our characteristic components, the experimental setup for generating and detecting THz radiation and the related results will be discussed.

3.2.1 Interdigital Photoconductive Antenna (IPCA)

The details of the PCA that we used for Terahertz generation will be explained in this part. Our PCA, shown in Fig.3.5, is an interdigital photoconductive terahertz antenna with a 2 THz resonance frequency, gap distance of 5 μm, active area of 1 mm x 1 mm, and optical excitation wavelength of λ= 800 nm. It has a prealigned hyperhemispherical silicon lens.

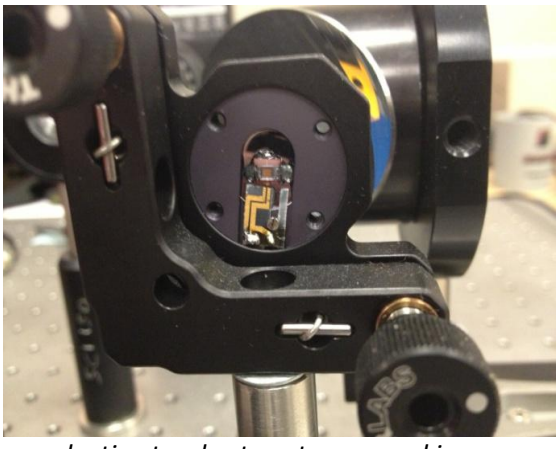

Figure 3. 5 *Interdigital photoconductive terahertz antenna used in our experiments.*

A photoconductive antenna (PCA) for terahertz (THz) waves consists of a highly resistive direct semiconductor thin film with two electric contact pads. The film is made in most cases using a III-V compound semiconductor like GaAs. It is epitaxially grown on a semi-insulating GaAs substrate (SI-GaAs), which is also a highly resistive material. The important difference between the SI-GaAs substrate and the film is the relaxation time for excited carriers. In a SI-substrate, the carrier lifetime is about 20 ps, but in the film it is shorter than 1 ps. To generate THz waves, a short laser pulse with a pulse width of less than 1 ps is focused between the electric contacts of the PCA. If the photons of the laser pulse have a photon energy larger than the energy gap E_g , they are absorbed in the film. Each absorbed photon creates a free electron in the conduction band and a hole in the valence band of the film. This excitation makes the semiconductor structure electrically conductive for a short time until the carriers are recombined.

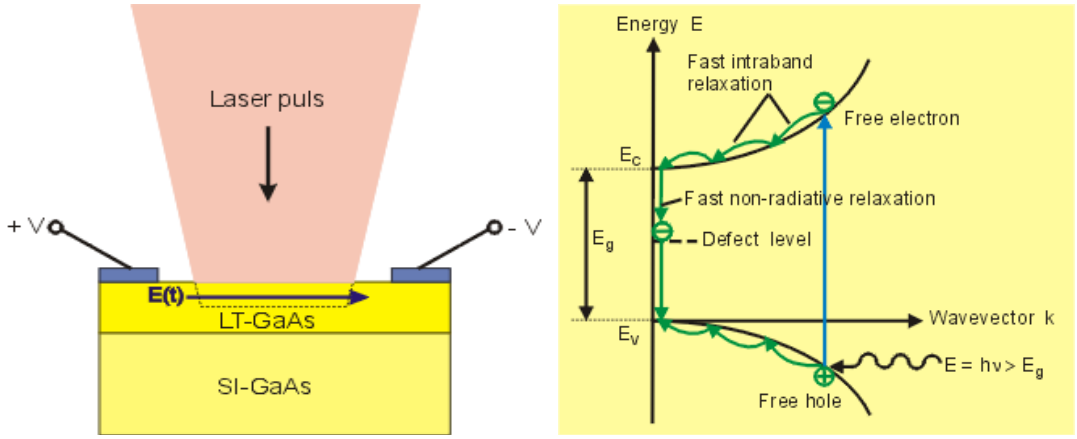

Figure 3. 6 *Schematic drawing of the structure of the IPCA and the energy diagram showing the generation of the electron hole pairs.(Taken from[78])*

To get the needed short carrier lifetime, the film must include crystal defects whose energy level is schematically shown in Fig.3.6. These defects can be created by ion implantation after the film growth or alternatively by a low temperature growth. Low temperature grown GaAs (LT-GaAs) between 200 and 400 °C contains excess arsenic clusters. These clusters create defect levels within the band gap and lead to a fast non-radiative recombination of the electron-hole pairs within a time interval of < 1 ps. The coherent

excitation of the single emitters located at every microlens spot results in a constructive interference of the radiated THz waves in the far field.

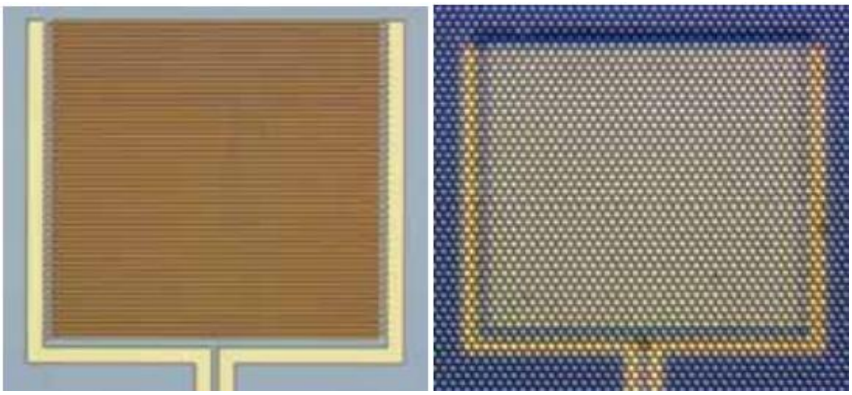

Figure 3. 7 *Top view of the IPCA metallic structure with a pre-aligned lens array.(Taken from [78])*

Because of the high refractive index (n ~ 3.4) of the semiconductor PCA, the outgoing terahertz waves are strongly diffracted at the substrate-air interface. Only the THz waves emitted in the solid angle Ω, given by

$$\Omega = 4\pi sin^2\left(\frac{\alpha}{2}\right) = 2\pi(1 - cos\alpha) = 2\pi(1 - \sqrt{\frac{n^2-1}{n^2}}) \quad (3.4)$$

with

α = arcsin (n^{-1})~17.1°

can escape the substrate. In Eq. (3.4), by using n=3.4 for GaAs, the escape solid angle Ω becomes 0.28 sterad. For GaAs with n = 3.4 the escape solid angle is Ω = 0.28. This is only 4.4% of the forward directed intensity(half of the sphere is 2π steradians).

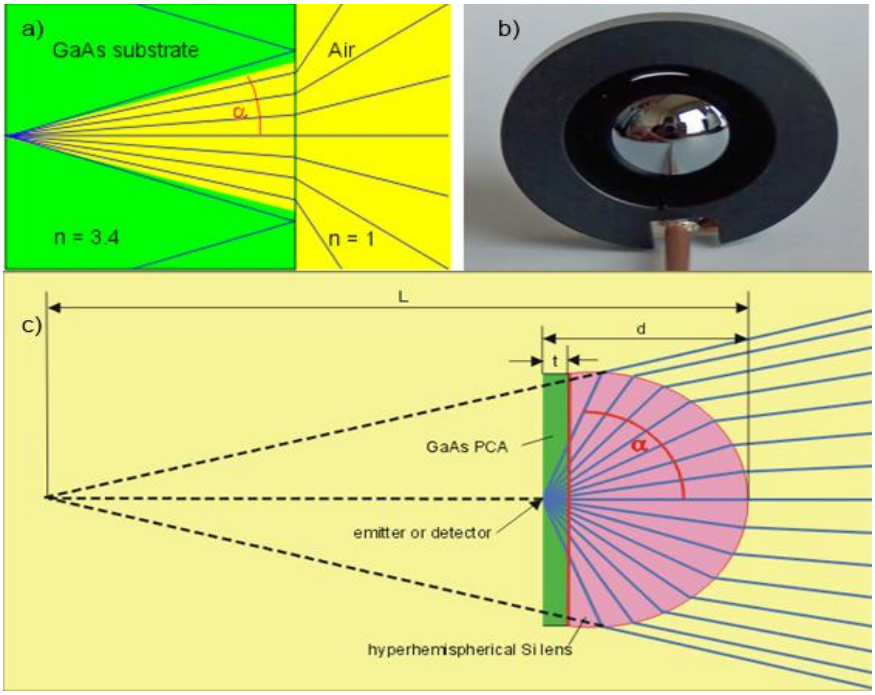

Figure 3.8 *a)PCA without substratelens b) Hyperhemispherical lens, c) Schematic drawing of the PCA with a hyperhemispherical lens.(Taken from [76])*

In order to increase the escape cone angle, a hemispherical lens with the same refractive index n as the PCA can be used. To decrease the divergence in air, a hyperhemispherical lens with a certain distance d from the emitter to the tip of the lens is used which is given by

$$d = r\left(\frac{n+1}{n}\right). \tag{3.5}$$

For a silicon lens with almost the same refractive index (n ~ 3.4) as GaAs at the therahertz frequencies, the distance is d = 1.29 r , where r is the lens radius. The height h of the aplanatic hyperhemispherical lens is therefore h = d – t , where t is the thickness t of the semiconductor PCA. The length L from the lens tip to the virtual focus behind the lens is given by

$$L = r(n+1) \tag{3.6}$$

For silicon, L = 4.4 r. With this hyperhemispherical lens, nearly all of the forward directed terahertz intensity can be collected and collimated after the PCA.

3.2.2 90- Degree Off-Axis Parabolic Mirror

The other characteristic components of our THz generation setup are the 90 Degree Off-Axis Parabolic Mirrors. We used two parabolic mirrors to collect, direct, and focus the terahertz radiation. The geometrical details and the reflectance curve of our parabolic mirrors are shown as in Figs. 3.9 and 3.10, respectively.

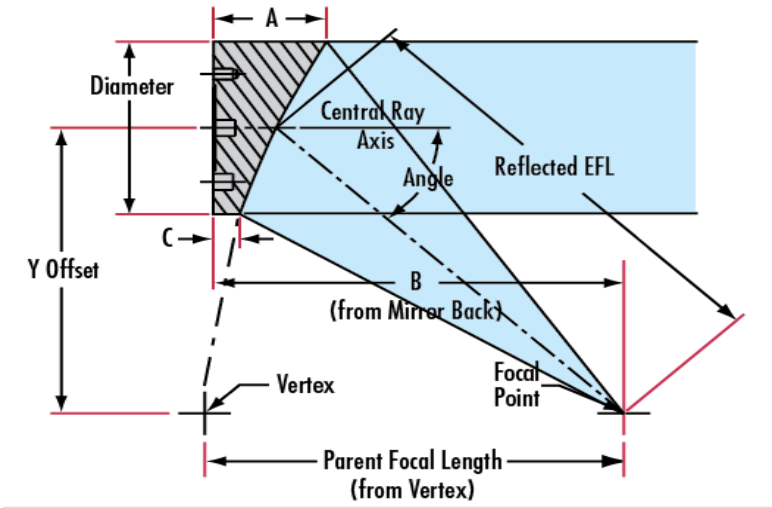

Figure 3. 9 *The geometric dimensions of the parabolic mirrors used for collimation and focusing of the THz waves with A=83.82mm, B=36.07mm, C=7.62mm, Diameter=76.2mm, Parent Focal Length=38.1mm, Effective Focal Length=76.2mm, and Y-Offset=76.2mm.*

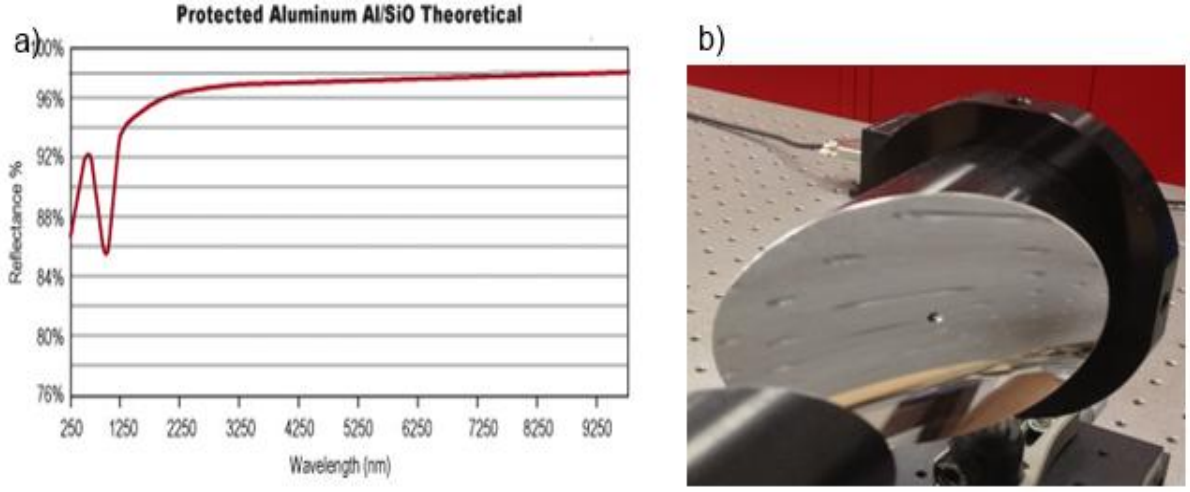

Figure 3. 10 *a)Reflectance Curve for the parabolic mirrors used in the THz collection experiment. b) Setup of our parabolic mirror pair for the collection and focusing of the THz waves.*

3.2.3 Ti:Sapphire Laser Cavity and Multipass-Cavity (MPC)

Teoretical background of the Multipass Cavity design was given in Chapter 1 of this thesis. In this section, the MPC design with the Ti:Sapphire laser cavity that we used for Terahertz generation will be presented.

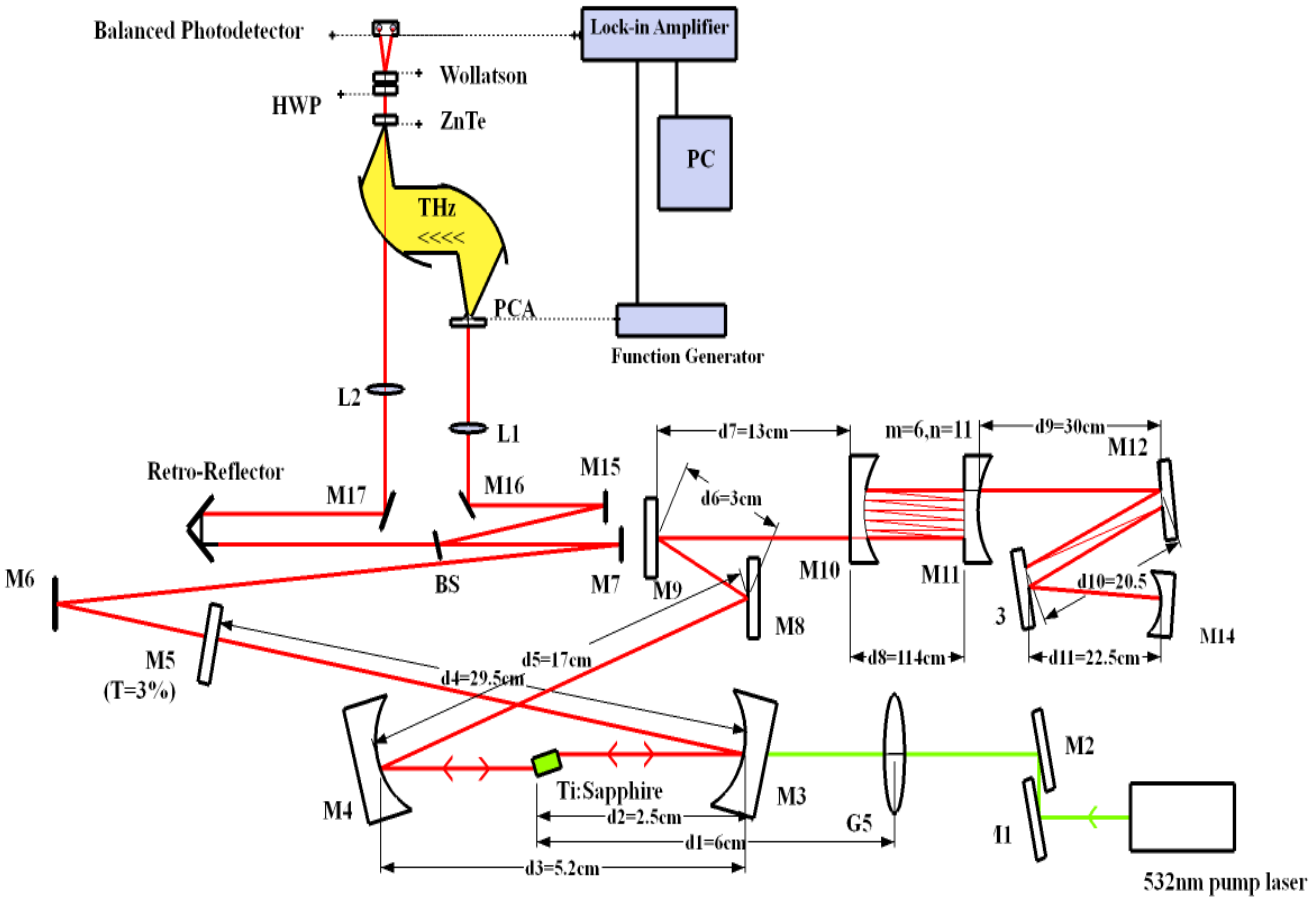

Figure 3. 11 *Schematic drawing of the experimental setup used to detect THz radiation by electro-optic sampling with the MPC Ti:Sapphire laser.*

In this configuration, as can be seen in Fig. 3.11, the lens (G5) with 50 mm focal length focuses the pump beam into the crystal. Two curved high reflectors (M3 and M4) each with radius of 50 mm were used for the cavity. The output coupler (M5) of 3% was used. The crystal was Brewster cut with fractional power absorption of 74% at the pump wavelength of 532nm. The mirrors (M3, M4, M8, M9) were used for dispersion compensation of the short cavity with a total negative group velocity dispersion(GVD) –of 410fs^2 . Additionally, we used two GTI mirors (M12, M13) for the extended cavity, each introducing a negative

dispersion of -500 fs^2 per reflection. In our optimum configuration (m=6 and n=11), the total cavity length is 26.6m. Assuming +20fs^2/m dispersion for the air and +200fs^2 for the crystal, the total GVD for the system using GTI mirrors came to around -1650fs^2.

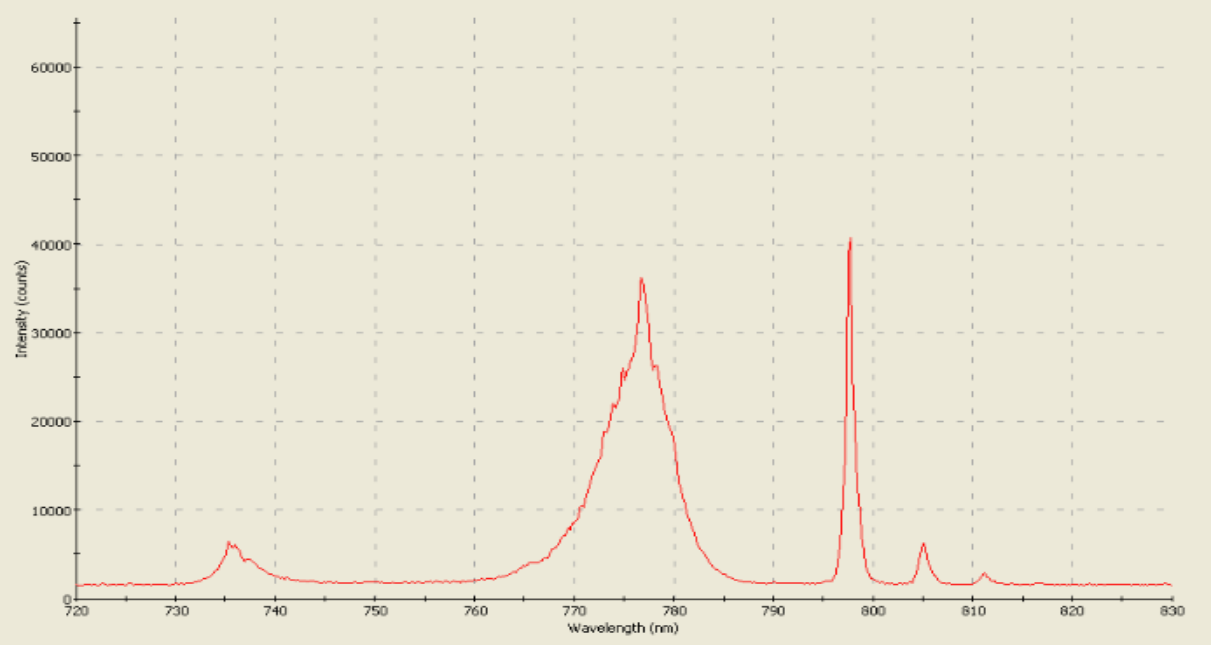

Figure 3. 12 *Spectrum of the femtosecond multi-pass cavity Ti:Sapphire Laser.*

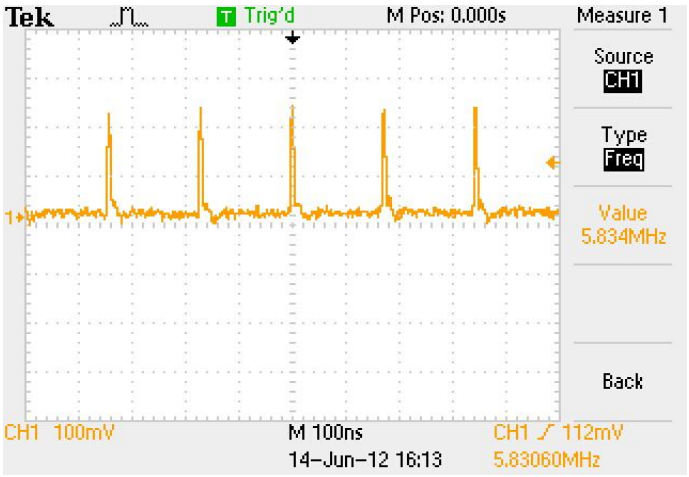

Figure 3. 13 *Pulse train of the MPC Ti:sapphire laser.*

Fig.3.12 shows the spectrum of the MPC Ti:sapphire laser during KLM operation. We measured the spectral bandwidth (FWHM) to be 7 nm. Fig.3.13 shows the pulse train for this configuration. The pulse train shows a stable single pulsed KLM operation of the system. We measured the pulse repetition rate as 5.83 MHz. The pulse width was 98 fs and the pulse energy was 30nJ. The pulsewidth was determined by assuming a sech^2 pulse profile. The time bandwidth product was 0.298[53].

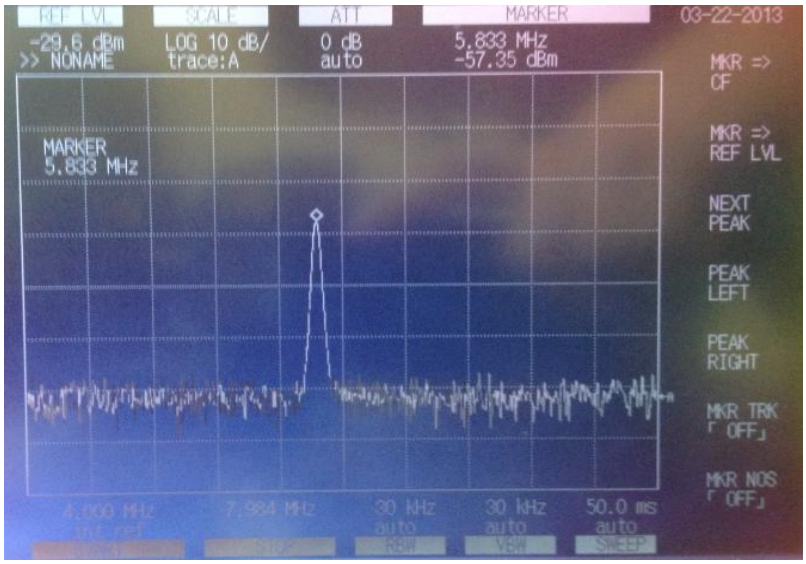

Figure 3. 14 *RF Spectrum of the femtpsecond MPC Ti:Sapphire laser.*

Further, the pulses also had a clean RF spectrum where the main peak at 5.833 MHz was more than 27 dB above the noise floor as can be seen in Fig. 3.14.

3.2.4 Results and Discussions

The experimental setup for generating and detecting THz radiation by electro optic sampling is shown in Fig. 3.15. The mode-locked Ti:sapphire laser producing 98 fs pulses at 800 nm with a 5.83 MHz repetition rate was used. By sending the output power of 100 mW (Ti:Sapphire beam) into the THz set up, we obtained 60-70 mW power on the generation arm just before the generation antenna and 3-5 mW power on the reference arm just after the 40 cm focusing lens.

We applied 10 V peak-to-peak sinusoidal voltage to our ICPA and used the nonlinear ZnTe crystal for electro optic detection. According to theory, when the optical reference pulse

travels through the crystal at the same time as one point in the THz pulse, it causes the detector crystal to become birefringent and the polarization of the sampling beam is slightly rotated. The magnitude of rotation is proportional to the magnitude of the THz field.

After the Wollaston prism, the reference beam was divided into two orthogonal linearly polarized outgoing beams as shown in Fig.3.15. However, because of the birefringence induced rotation, the beam is not separated equally and this is detected as a voltage difference by the balanced photodetector. Then, the signal is collected with a lock-in amplifier phase-locked to an optical chopper, which modulates the THz generation arm.

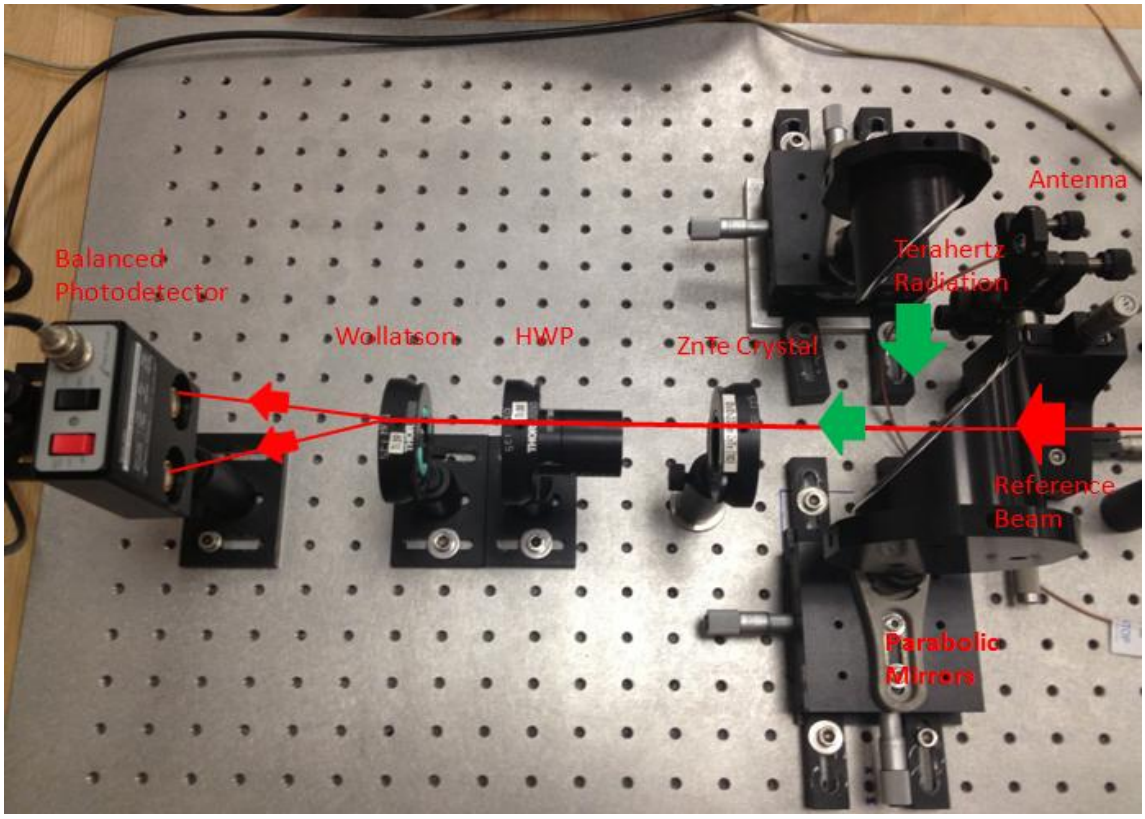

Figure 3. 15 *Electro-optic detection mechanism where the THz induced birefringence is sensed as a voltage difference.*

The terahertz signal could not be detected by the electro optic sampling method. The possible reasons could be as follows. The expected signal was in the range of 200μV which is easily subject to be lost in the noise level even when we used a lock in amplifier. The continuous oscillations that we saw in the lock in amplifier display might be inferring a locking related

problem or a noise problem that we could not eliminate in our system. Another reason might be that the terahertz radiation was not intense enough to create a measurable birefringence in the ZnTe nonlinear crystal

After trying different configurations for detecting THz radiation by electro-optic sampling, we decided to try the antenna detection method. The scheme of the detection method by using PCA is shown in Fig. 3.16. In this configuration, we again used the same ICPA in the generation arm. However, another PCA was used for detection in the reference arm. Detection PCA was excited and electron hole pairs were created by the reference beam. The excited carriers are accelerated by the electric field component of the incident terahertz pulse with the time-dependent electrical field E(t). This leads to a measurable current signal in the outer circuit.

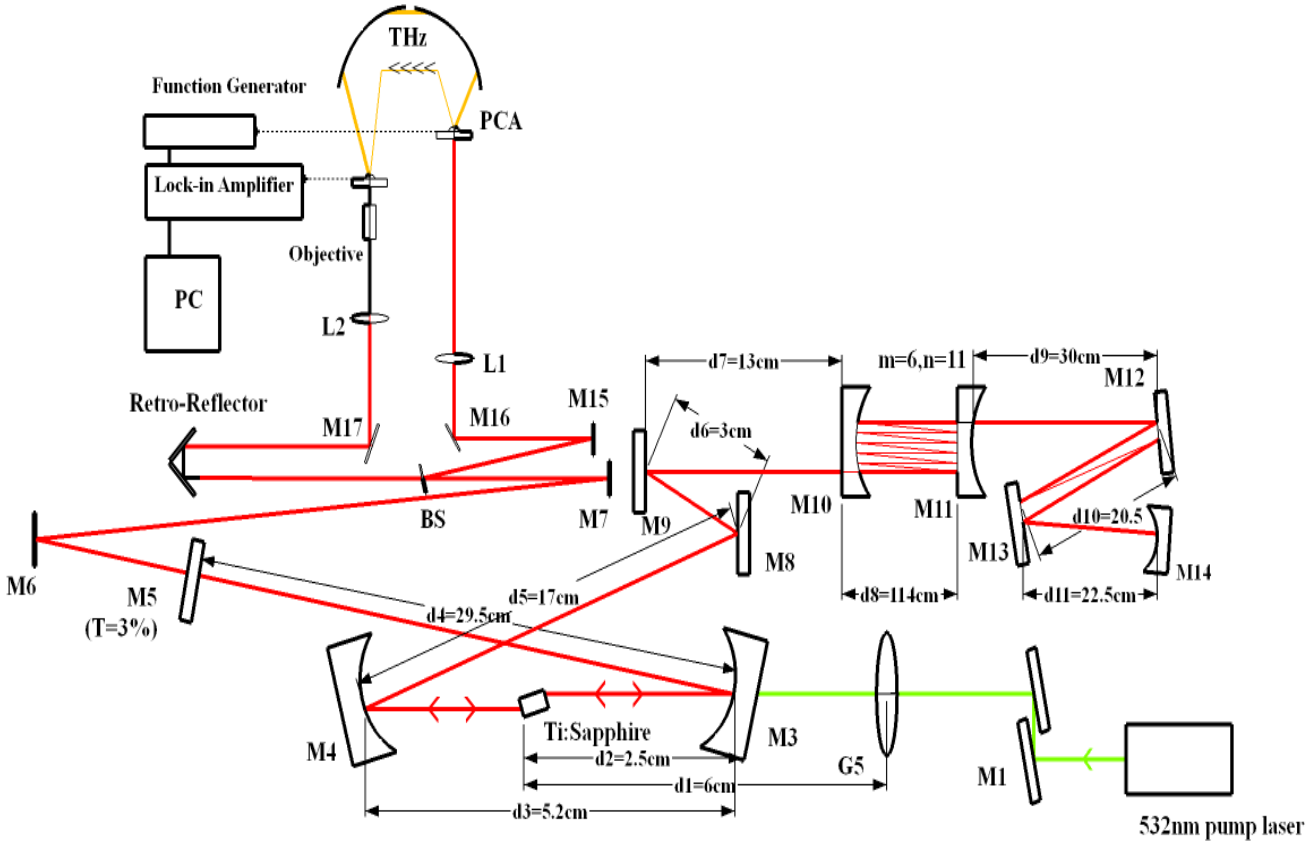

Figure 3. 16 *Schematic drawing of the experimental setup used to detect THz radiation with a photo-conductive antenna.*

Photoconductive antennas have superior detection responsivity and their signal-to-noise ratios are typically far better than electro optic sampling [65, 75]. We could detect the THz pulse for which the intensity is around 5mV with a bandgap of approximately 0.6 THz by using another PCA for detection as shown in Fig.3.18. From the point of view of the intensity, the measurement provide a sufficiently large signal. However, the bandwidth of the obtained pulse was not sufficient for Terahertz Time Domain Spectroscopy. This might be a result of the mismatch in the spectral responsivity between the generation and the detection antennas.

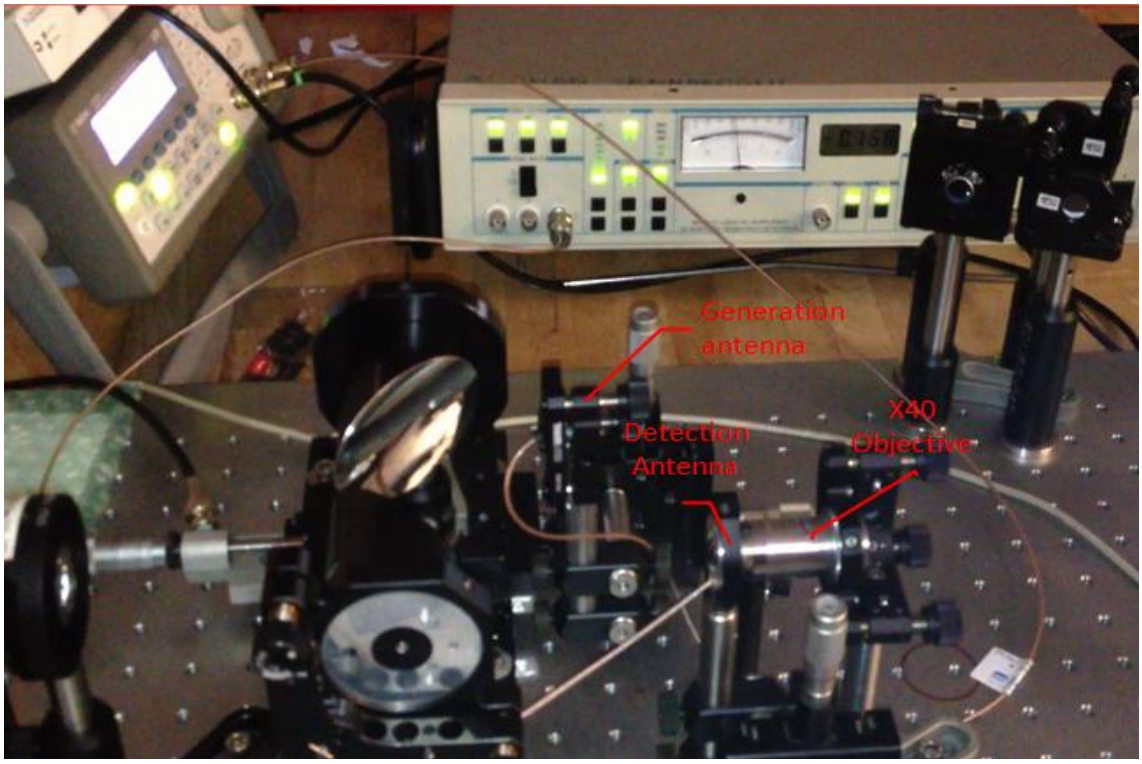

Figure 3. 17 *A photograph of the setup used for THz detection with the PCA.*

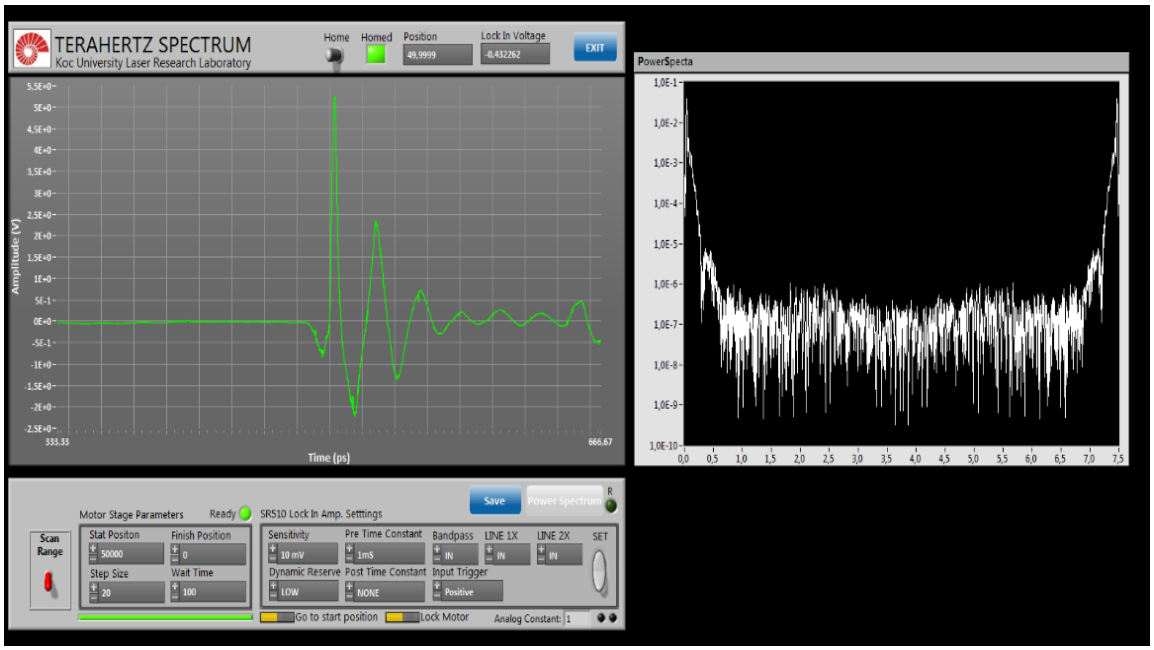

Figure 3. 18 *THz Pulse detected by antenna-antenna detection method and its spectrum with a bandwidth of approximately 0.6 THz.*

In summary, we could succesfully generate and detecte THz radiation with the antenna- antenna configuration. However, the detection attempts with electro optic sampling method were not successful. At that point, more detailed noise elimination methods can be applied for the setup. Because, we are somehow losing the signal that is expected to be in the range of ~200μV. For the antenna detection case, the bandwidth of the obtained pulse should be improved in order to establish a terahertz Time Domain Spectroscopy system. This might be achieved via a detection antenna which is identical to the generation antenna so that the matching between the antennas will be improved and better results can be obtained.

Chapter 4: Conclusions

In this thesis work, some key concepts that play a critical role in the understanding of the experimental parts of the thesis were first introduced. A brief background about geometrical optics was presented and a useful matrix formalism for the analysis of complex optical systems in the paraxial approximation regime was applied to the analysis of the multipass-cavity. Then, four level atomic systems and Q-switching condition with a saturable absorber were discussed. Furthermore, a concise review of some important nonlinear interactions such as Kerr lens mode locking, group delay dispersion and self phase modulation were covered.

In the second part of the thesis, a directly diode pumped, low cost, and highly efficient 800-nm Cr:LiCAF laser which can be operated above 100 MHz was designed and demonstrated experimentally with the goal of developing high repetition rate oscillators for frequency comb applications. A semiconductor Bragg reflector (SBR) was added into the resonator to initiate the mode- locked operation of the laser. In the experiments, a four mirror x-cavity laser containing a 7% doped Cr:LiCAF crystal was end pumped with a recently developed high brightness, 1-W tapered diode at 675 nm. By using 915 mW of pump power, 340 fs pulses around 800 nm with an output power of 50 mW were produced at a repetition rate of 120 MHz. A second tapered diode was added into the system to reach higher frequencies. However, above 200MHz repetition rates, it was observed that the tight focusing and the energy of the pulse on the SBR caused damage of the SBR. Based on previous studies, we believe that there is a great potential to reduce this thermal damage in future studies. Furthermore, the availability of tapered diode pump sources with higher electrical to optical conversion efficiencies is expected to increase the output power of the laser and make it possible to obtain high repetition rates up to or beyond 1 GHz. Our future research efforts will focus on obtaining GHz level pulses with sub-100-fs duration at average powers around 100 mW.

In the third part of the thesis, a home-built multi-pass cavity femtosecond Ti:Sapphire laser, which generated 98 fs pulses with a repetition rate of 5.53 MHz at 776 nm, was used to generate THz radiation from a photoconductive antenna. This was achieved by focusing the output of the Ti:Sapphire laser with an average power of 60-70 mW on a photoconductive antenna made of low-temperature grown GaAs (Lt-GaAs) . The signal strength of the generated THz waves was 5 mV and they were in the frequency range of 0.1-0.7 THz as detected by a second photoconductive antenna. With improved antenna and detection design, we expect to further improve the bandwidth and efficiency of THz generation with the multipass-cavity Ti:sapphire laser.

Appendix A: Autocorrelation Measurement

It is not possible to measure the duration of ultra short optical pulses with the current electronic measurement systems. Measuring these optical pulses is possible with an autocorrelator. In this section, the operation of the autocorrelator for pulsewidth characterization is described. Figure A1 shows the autocorrelator setup that we used for measuring the pulse durations. The setup consists of a Michelson interferometer, a non-linear crystal for second harmonic generation, and a detector.

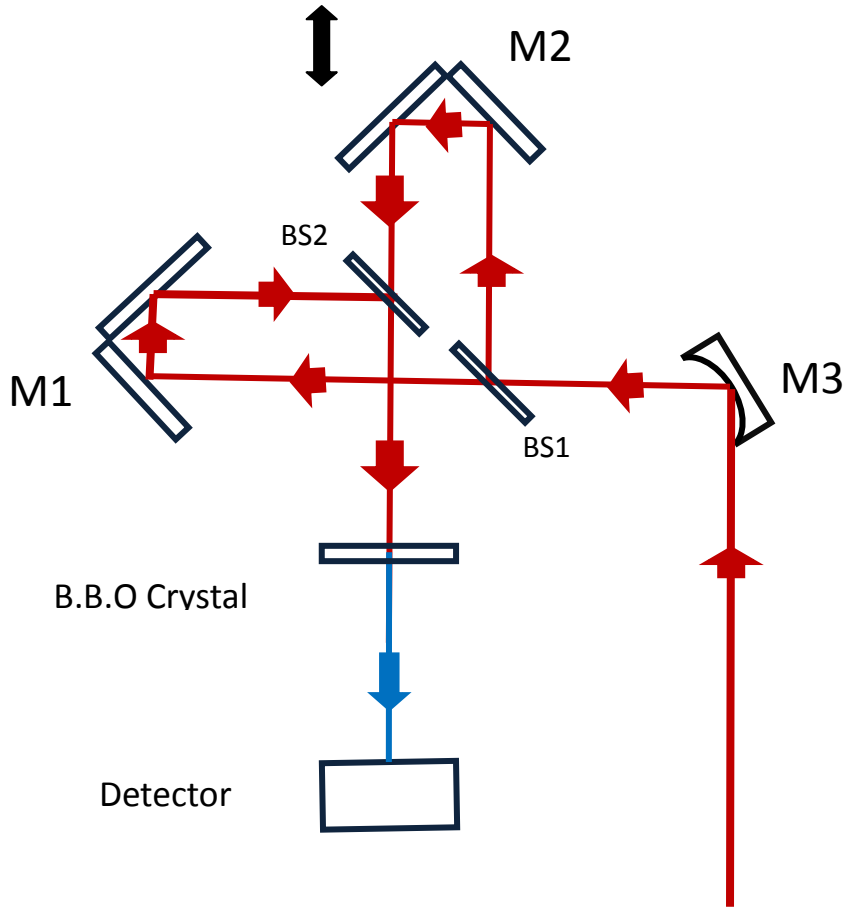

Fig.A1 *Schematic for the autocorrelator setup used for ultrashort pulse duration measurements*

The beam coming from the output of the Cr^{3+}: LiCAF laser was split into two parts by the first beam splitter (BS1). One travels to the movable mirror(M2) which is periodically driven to change the delay between the two pulse trains and the other travels to the fixed mirror (M1). Thus, The reflected pulses recombine on the second beam splitter (BS2) and then are focused inside the non-linear crystal (BBO crystal). When the two arms of the interferometer becomes equal by changing the position of the mirror M1, the collinear beams lead to second harmonic generation inside the nonlinear crystal. After the crystal, the intensity of the generated second harmonic signal is detected with a silicon detector. Since the second harmonic instensity is proportional to the product of the intensity in one arm and the delayed intensity in the other arm, it can be shown that with a slow detector, the second harmonic signal corresponds to the autocorrelation of the pulse intensity. Hence, by assuming a suitable intensity profile for the pulses (typically $sech^2$ intensity profile), the actual duration of the pulses can be determined.

VITA

Can Cihan received his B.S. degree from the Department of Electrical and Electronics Engineering at Eastern Mediterranean University, Famagusta, Cyprus as the valedictorian of the Engineering Faculty. During his undergraduate period, he worked with Dr. Dizem Arifler on the simulation of photon propagation through nanoparticle-labeled epithelial tissues. He worked as an intern at the Biomedical Engineering Institute of Bogazici University, where he studied basic theoretical principles of light-tissue interaction and carried out experiments with tissue-simulating phantoms to analyze light transport under the supervision of Dr. Ata Akın. He was in the M.S. program of the Department of Electrical and Electronics Engineering at Bilkent University and studied with Dr. Özgür Aktaş on carbon nanotube(CNT) DNA sensing transistors. Then, he started his M.S. studies in Optoelectronics and Photonics Engineering at Koc University under the supervision of Prof. Alphan Sennaroğlu. He will continue his PhD work in the Department of Electrical and Electronics Engineering at Koc University. His interests include compact diode-pumped femtosecond solid-state lasers and terahertz time domain spectroscopy.

Publications:

- C. Cihan and D. Arifler, "Influence of phase function on modeled optical response of Nanoparticlelabeledepithelialtissues,"*JournalofBiomedicalOptics*,16(8),085002,(2011).

BIBLIOGRAPHY

1. Young, M.D., et al., *Multiphoton imaging with a direct ‐diode pumped femtosecond Ti: sapphire laser.* Journal of microscopy, 2013. **249**(2): p. 83-86.
2. Saha, K., et al., *Modelocking and femtosecond pulse generation in chip-based frequency combs.* Opt. Express, 2013. **21**(1): p. 1335-1343.
3. Popmintchev, T., et al., *Bright Coherent Ultrahigh Harmonics in the keV X-ray Regime from Mid-Infrared Femtosecond Lasers.* Science, 2012. **336**(6086): p. 1287-1291.
4. Marian, A., et al., *United Time-Frequency Spectroscopy for Dynamics and Global Structure.* Science, 2004. **306**(5704): p. 2063-2068.
5. Fu, D., et al., *Hyperspectral Imaging with Stimulated Raman Scattering by Chirped Femtosecond Lasers.* The Journal of Physical Chemistry B, 2012. **117**(16): p. 4634-4640.
6. Ye, J. and S.T. Cundiff, *Femtosecond Optical Frequency Comb: Principle, Operation and Applications*. 2005: Springer.
7. Gerrard, A. and J.M. Burch, *Introduction to matrix theory methods in optics*. 1975: DOVER PUBN Incorporated.
8. Sennaroglu, A., *Photonics and Laser Engineering: Principles, Devices, and Applications*. 2010: McGraw-Hill Education.
9. Herriott, D., H. Kogelnik, and R. Kompfner, *Off-Axis Paths in Spherical Mirror Interferometers.* Appl. Opt., 1964. **3**(4): p. 523-526.
10. Sennaroglu, A. and J. Fujimoto, *Design criteria for Herriott-type multi-pass cavities for ultrashort pulse lasers.* Opt. Express, 2003. **11**(9): p. 1106-1113.
11. Sennaroglu, A., et al., *Compact femtosecond lasers based on novel multipass cavities.* Quantum Electronics, IEEE Journal of, 2004. **40**(5): p. 519-528.
12. Cho, S.H., et al., *Low-repetition-rate high-peak-power Kerr-lens mode-locked TiAl2O3 laser with a multiple-pass cavity.* Opt. Lett., 1999. **24**(6): p. 417-419.
13. Saleh, B.E.A. and M.C. Teich, *Fundamentals of Photonics*. 2013: Wiley.
14. Keller, U., et al., *Semiconductor saturable absorber mirrors (SESAM's) for femtosecond to nanosecond pulse generation in solid-state lasers.* Selected Topics in Quantum Electronics, IEEE Journal of, 1996. **2**(3): p. 435-453.
15. Tsuda, S., et al., *Mode-locking ultrafast solid-state lasers with saturable Bragg reflectors.* Selected Topics in Quantum Electronics, IEEE Journal of, 1996. **2**(3): p. 454-464.
16. Spühler, G.J., et al., *Experimentally confirmed design guidelines for passively Q-switched microchip lasers using semiconductor saturable absorbers.* J. Opt. Soc. Am. B, 1999. **16**(3): p. 376-388.
17. Kaertner, F.X., et al., *Control of solid state laser dynamics by semiconductor devices.* Optical Engineering, 1995. **34**(7): p. 2024-2036.
18. Hentschel, M., et al., *Attosecond metrology.* Nature, 2001. **414**(6863): p. 509-513.
19. Boyd, R.W., *Nonlinear Optics*. 2003: Acad. Press.
20. Sennaroglu, A., *Solid-State Lasers and Applications*. 2010: Taylor & Francis.
21. Yariv, A. and P. Yeh, *Photonics: Optical Electronics in Modern Communications*. 2007: Oxford University Press, Incorporated.
22. Kerr, J., *LIV. A new relation between electricity and light: Dielectrified media birefringent (Second paper).* Philosophical Magazine Series 4, 1875. **50**(333): p. 446-458.
23. Quimby, R.S., *Photonics and Lasers: An Introduction*. 2006: Wiley.

24. Stingl, A., et al., *Generation of 11-fs pulses from a Ti:sapphire laser without the use of prisms.* Opt. Lett., 1994. **19**(3): p. 204-206.
25. Qian, L.J., X. Liu, and F.W. Wise, *Femtosecond Kerr-lens mode locking with negative nonlinear phase shifts.* Opt. Lett., 1999. **24**(3): p. 166-168.
26. Wagenblast, P.C., et al., *Generation of sub-10-fs pulses from a Kerr-lens mode-locked Cr3+:LiCAF laser oscillator by use of third-order dispersion-compensating double-chirped mirrors.* Opt. Lett., 2002. **27**(19): p. 1726-1728.
27. Sorokina, I.T., et al., *14-fs pulse generation in Kerr-lens mode-locked prismless Cr:LiSGaF and Cr:LiSAF lasers: observation of pulse self-frequency shift.* Opt. Lett., 1997. **22**(22): p. 1716-1718.
28. Cizmeciyan, M.N., et al., *Kerr-lens mode-locked femtosecond Cr2+:ZnSe laser at 2420 nm.* Opt. Lett., 2009. **34**(20): p. 3056-3058.
29. Roth, P.W., et al., *Directly diode-laser-pumped Ti:sapphire laser.* Opt. Lett., 2009. **34**(21): p. 3334-3336.
30. Harrison, J., et al., *Low-threshold, cw, all-solid-state Ti:Al2O3 laser.* Opt. Lett., 1991. **16**(8): p. 581-583.
31. Payne, S.A., et al., *LiCaAlF₆:Cr³⁺: a promising new solid-state laser material.* Quantum Electronics, IEEE Journal of, 1988. **24**(11): p. 2243-2252.
32. Scheps, R., et al., *Diode-pumped Cr:LiSrAlF6 laser.* Opt. Lett., 1991. **16**(11): p. 820-822.
33. Valentine, G.J., et al., *Ultralow-pump-threshold, femtosecond Cr(3+):LiSrAlF(6)laser pumped by a single narrow-stripe AlGaInP laser diode.* Opt Lett, 1997. **22**(21): p. 1639-41.
34. Druon, F., F. Balembois, and P. Georges, *New laser crystals for the generation of ultrashort pulses.* Comptes Rendus Physique, 2007. **8**(2): p. 153-164.
35. Lacayo, G., et al., *Transmission Electron Microscope Study of Secondary Phases in Cr3+:LiCaAlF6 Single Crystals.* Crystal Research and Technology, 1999. **34**(9): p. 1221-1227.
36. Klimm, D. and P. Reiche, *Ternary Colquiriite Type Fluorides as Laser Hosts.* Crystal Research and Technology, 1999. **34**(2): p. 145-152.
37. Klimm, D., G. Lacayo, and P. Reiche, *Growth of Cr : LiCaAlF6 and Cr : LiSrAlF6 by the Czochralski method.* Journal of Crystal Growth, 2000. **210**(4): p. 683-693.
38. Klimm, D., R. Uecker, and P. Reiche, *Melting behavior and growth of colquiriite laser crystals.* Crystal Research and Technology, 2005. **40**(4-5): p. 352-358.
39. Kopf, D., et al., *High-average-power diode-pumped femtosecond Cr:LiSAF lasers.* Applied Physics B, 1997. **65**(2): p. 235-243.
40. Eichenholz, J.M. and M. Richardson. *Measurement of Thermal Lensing in Cr3+ doped Colquiriites*. 1998. Optical Society of America.
41. Keller, U., et al., *Solid-state low-loss intracavity saturable absorber for Nd:YLF lasers: an antiresonant semiconductor Fabry?Perot saturable absorber.* Opt. Lett., 1992. **17**(7): p. 505-507.
42. Demirbas, U., et al., *Femtosecond Cr:LiSAF and Cr:LiCAF lasers pumped by tapered diode lasers.* Opt. Express, 2011. **19**(21): p. 20444-20461.
43. French, P.M.W., et al., *Mode-locked all-solid-state diode-pumped Cr:LiSAF laser.* Opt. Lett., 1993. **18**(22): p. 1934-1936.
44. Isemann, A. and C. Fallnich, *High-power Colquiriite lasers with high slope efficiencies pumped by broad-area laser diodes.* Opt. Express, 2003. **11**(3): p. 259-264.
45. Demirbas, U., et al., *Diode-pumped, high-average-power femtosecond Cr3+:LiCAF laser.* Opt. Lett., 2007. **32**(22): p. 3309-3311.
46. Demirbas, U., et al., *Comparative investigation of diode pumping for continuous-wave and mode-locked Cr3+:LiCAF lasers.* J. Opt. Soc. Am. B, 2009. **26**(1): p. 64-79.

47. Demirbas, U., et al., *Low-cost, single-mode diode-pumped Cr:Colquiriite lasers.* Opt. Express, 2009. **17**(16): p. 14374-14388.
48. Agate, B., et al., *Simplified cavity designs for efficient and compact femtosecond Cr:LiSAF lasers.* Optics Communications, 2002. **205**(1–3): p. 207-213.
49. Tsuda, S., W.H. Knox, and S.T. Cundiff, *High efficiency diode pumping of a saturable Bragg reflector-mode-locked Cr:LiSAF femtosecond laser.* Applied Physics Letters, 1996. **69**(11): p. 1538-1540.
50. Hopkins, J.M., et al., *Highly compact and efficient femtosecond Cr:LiSAF lasers.* Quantum Electronics, IEEE Journal of, 2002. **38**(4): p. 360-368.
51. Hopkins, J.M., et al., *Efficient, low-noise, SESAM-based femtosecond Cr3+:LiSrAlF6 laser.* Optics Communications, 1998. **154**(1–3): p. 54-58.
52. Demirbas, U., et al., *Highly Efficient, Low-Cost Diode-Pumped Femtosecond Cr3+:LiCAF Lasers*, in *Ultrafast Phenomena XVI*, P. Corkum, et al., Editors. 2009, Springer Berlin Heidelberg. p. 753-755.
53. Demirbas, U., et al., *Femtosecond tuning of Cr:colquiriite lasers with AlGaAs-based saturable Bragg reflectors.* J. Opt. Soc. Am. B, 2011. **28**(5): p. 986-993.
54. Li, D., et al., *Diode-pumped passively mode-locked GHz femtosecond Cr:LiSAF laser with kW peak power.* Opt Lett, 2010. **35**(9): p. 1446-8.
55. Sumpf, B., et al., *High-Brightness Quantum Well Tapered Lasers.* Selected Topics in Quantum Electronics, IEEE Journal of, 2009. **15**(3): p. 1009-1020.
56. Sumpf, B., et al., *Nearly Diffraction-Limited Tapered Lasers at 675 nm With 1-W Output Power and Conversion Efficiencies Above 30%.* Photonics Technology Letters, IEEE, 2011. **23**(4): p. 266-268.
57. Hönninger, C., et al., *Q-switching stability limits of continuous-wave passive mode locking.* J. Opt. Soc. Am. B, 1999. **16**(1): p. 46-56.
58. Ferguson, B. and X.-C. Zhang, *Materials for terahertz science and technology.* Nat Mater, 2002. **1**(1): p. 26-33.
59. Auston, D.H., K.P. Cheung, and P.R. Smith, *Picosecond photoconducting Hertzian dipoles.* Applied Physics Letters, 1984. **45**(3): p. 284-286.
60. Smith, P.R., D.H. Auston, and M.C. Nuss, *Subpicosecond photoconducting dipole antennas.* Quantum Electronics, IEEE Journal of, 1988. **24**(2): p. 255-260.
61. Exter, M.v., C. Fattinger, and D. Grischkowsky, *Terahertz time-domain spectroscopy of water vapor.* Opt. Lett., 1989. **14**(20): p. 1128-1130.
62. Ketchen, M.B., et al., *Generation of subpicosecond electrical pulses on coplanar transmission lines.* Applied Physics Letters, 1986. **48**(12): p. 751-753.
63. Grischkowsky, D., et al., *Far-infrared time-domain spectroscopy with terahertz beams of dielectrics and semiconductors.* J. Opt. Soc. Am. B, 1990. **7**(10): p. 2006-2015.
64. Kono, S., et al., *Detection of up to 20 THz with a low-temperature-grown GaAs photoconductive antenna gated with 15 fs light pulses.* Applied Physics Letters, 2000. **77**(25): p. 4104-4106.
65. Kono, S., M. Tani, and K. Sakai, *Ultrabroadband photoconductive detection: Comparison with free-space electro-optic sampling.* Applied Physics Letters, 2001. **79**(7): p. 898-900.
66. Kono, S., M. Tani, and K. Sakai, *Coherent detection of mid-infrared radiation up to 60 THz with an LT-GaAs photoconductive antenna.* Optoelectronics, IEE Proceedings -, 2002. **149**(3): p. 105-109.
67. Sakai, K., *Terahertz Optoelectronics*. 2005: Springer.
68. Duvillaret, L., et al., *Analytical modeling and optimization of terahertz time-domain spectroscopy experiments, using photoswitches as antennas.* Selected Topics in Quantum Electronics, IEEE Journal of, 2001. **7**(4): p. 615-623.

69. Han, P.Y. and X.C. Zhang, *Coherent, broadband midinfrared terahertz beam sensors.* Applied Physics Letters, 1998. **73**(21): p. 3049-3051.
70. Reimann, K., et al., *Direct field-resolved detection of terahertz transients with amplitudes of megavolts per centimeter.* Opt Lett, 2003. **28**(6): p. 471-3.
71. Han, P.Y., G.C. Cho, and X.C. Zhang, *BROAD BAND MID-INFRARED THz PULSE: MEASUREMENT TECHNIQUE AND APPLICATIONS.* Journal of Nonlinear Optical Physics & Materials, 1999. **08**(01): p. 89-105.
72. Huber, R., et al., *Generation and field-resolved detection of femtosecond electromagnetic pulses tunable up to 41 THz.* Applied Physics Letters, 2000. **76**(22): p. 3191-3193.
73. Wu, Q. and X.C. Zhang, *Free-space electro-optic sampling of terahertz beams.* Applied Physics Letters, 1995. **67**(24): p. 3523-3525.
74. Gallot, G. and D. Grischkowsky, *Electro-optic detection of terahertz radiation.* Journal of the Optical Society of America B-Optical Physics, 1999. **16**(8): p. 1204-1212.
75. Cai, Y., et al., *Coherent terahertz radiation detection: Direct comparison between free-space electro-optic sampling and antenna detection.* Applied Physics Letters, 1998. **73**(4): p. 444-446.

76 Broad area interdigital photoconductive THz antenna with microlens array and hyperhemispherical silicon lens for laser excitation wavelengths λ ~ 800 nm Retrieved,Septe mber 1,2013 from http://www.batop.de/

77. Mostafazadeh A. 2010,*Pulse Energy Optimization In Multipass-Cavity Mode-Locked Femtosecond Lasers,* M.Sc. Thesis,Koc University

78. Tapered Diode Lasers - Efficient, High Brightness Light Sources. Retrieved,September 1,2013 fromhttp://www.fbh-berlin.de/willkommen